AGU ADVANCING EARTH AND SPACE SCIENCE

Space Weather®

RESEARCH ARTICLE
10.1029/2022SW003101

Significant Ionospheric Hole and Equatorial Plasma Bubbles After the 2022 Tonga Volcano Eruption

Ercha Aa[1], Shun-Rong Zhang[1], Philip J. Erickson[1], Juha Vierinen[2], Anthea J. Coster[1], Larisa P. Goncharenko[1], Andres Spicher[2], and William Rideout[1]

[1]Haystack Observatory, Massachusetts Institute of Technology, Westford, MA, USA, [2]Department of Physics and Technology, The Arctic University of Norway, Tromsø, Norway

Key Points:

- Shock-acoustic impulses created a significant ionospheric hole of 10+ TECU depletion near the epicenter, with an estimated radius of 10–15°
- Pronounced post-volcanic equatorial plasma bubbles were continuously developed across the Asia-Oceania area covering ~140° longitudes
- Strong plasma bubbles were likely triggered by gravity wave resonance with Lamb waves and volcano-increased PRE/PSSR of equatorial F-layer

Supporting Information:

Supporting Information may be found in the online version of this article.

Correspondence to:

E. Aa,
aercha@mit.edu

Citation:

Aa, E., Zhang, S.-R., Erickson, P. J., Vierinen, J., Coster, A. J., Goncharenko, L. P., et al. (2022). Significant ionospheric hole and equatorial plasma bubbles after the 2022 Tonga volcano eruption. *Space Weather*, *20*, e2022SW003101. https://doi.org/10.1029/2022SW003101

Received 22 MAR 2022
Accepted 22 JUN 2022

Abstract This paper investigates the local and global ionospheric responses to the 2022 Tonga volcano eruption, using ground-based Global Navigation Satellite System total electron content (TEC), Swarm in situ plasma density measurements, the Ionospheric Connection Explorer (ICON) Ion Velocity Meter (IVM) data, and ionosonde measurements. The main results are as follows: (a) A significant local ionospheric hole of more than 10 TECU depletion was observed near the epicenter ~45 min after the eruption, comprising of several cascading TEC decreases and quasi-periodic oscillations. Such a deep local plasma hole was also observed by space-borne in situ measurements, with an estimated horizontal radius of 10–15° and persisted for more than 10 hr in ICON-IVM ion density profiles until local sunrise. (b) Pronounced post-volcanic evening equatorial plasma bubbles (EPBs) were continuously observed across the wide Asia-Oceania area after the arrival of volcano-induced waves; these caused a N_e decrease of 2–3 orders of magnitude at Swarm/ICON altitude between 450 and 575 km, covered wide longitudinal ranges of more than 140°, and lasted around 12 hr. (c) Various acoustic-gravity wave modes due to volcano eruption were observed by accurate Beidou geostationary orbit (GEO) TEC, and the huge ionospheric hole was mainly caused by intense shock-acoustic impulses. TEC rate of change index revealed globally propagating ionospheric disturbances at a prevailing Lamb-wave mode of ~315 m/s; the large-scale EPBs could be seeded by acoustic-gravity resonance and coupling to less-damped Lamb waves, under a favorable condition of volcano-induced enhancement of dusktime plasma upward E×B drift and postsunset rise of the equatorial ionospheric F-layer.

Plain Language Summary The catastrophic 2022 Tonga volcano eruption triggered giant atmospheric waves that propagated into and strongly impacted Earth's ionosphere. Using ground-based multi-Global Navigation Satellite System total electron content (TEC) and ionosonde measurements as well as space-borne Swarm and Ionospheric Connection Explorer satellites observations, we found large-scale, intense ionospheric disturbances. The eruption created a large ionospheric hole near the epicenter embedded with cascading TEC drops and periodic oscillations, resulting from various shock-acoustic wave impulses. Atmospheric Lamb waves propagated globally at a velocity of ~315 m/s, coupled to ionosphere heights possibly via acoustic-gravity resonance, and caused global-scale ionospheric disturbances. We report for the first time that strong nighttime equatorial plasma bubbles were continuously observed over the vast Asia-Oceania area of more than 140° longitudinal range, lasting around 12 hr following the consecutive arrival of volcano-induced waves and the dusk terminator. These results demonstrate far-reaching and long-lasting atmosphere-ionosphere impacts from a devastating natural disaster, and highlight new ways in which surface conditions can impact the upper atmosphere.

1. Introduction

Natural geological disasters such as volcanic eruptions and intense earthquakes can create impulsive forcing near Earth's surface and cause considerable atmospheric pressure waves (e.g., Hines, 1960; Komjathy et al., 2016; Yeh & Liu, 1974). Depending on their velocities and/or frequencies, these atmospheric waves include supersonic shock waves along with acoustic and gravity waves (AGWs). Acoustic waves travel through adiabatic compression and decompression, with frequencies higher than the acoustic cutoff frequency (~3.3 mHz), periods smaller than 5 min, and radially outward propagating velocity at the sound speed (Astafyeva, 2019; Blanc, 1985). By comparison, gravity waves are triggered by vertical displacement in the ocean surface and atmosphere, with gravity being the predominant restoring force. They are characterized by lower-than-buoyancy frequencies, periods of several to tens of minutes, and obliquely upward propagating pattern with oppositely directed phase and

group velocities (Artru et al., 2004; Huang et al., 2019). The initial AGWs generated by these events can even reach ionospheric heights with exponentially increased amplitudes, modulating ionospheric electron density and leading to traveling ionospheric disturbances (TIDs) through ion-neutral collisional momentum transfer (e.g., Afraimovich et al., 2010; Cahyadi & Heki, 2013; Chou et al., 2020; Dautermann, Calais, & Mattioli, 2009; Hao et al., 2006; Huba et al., 2015; Inchin et al., 2020; Komjathy et al., 2012; Liu et al., 2006; Nishioka et al., 2013; Rolland et al., 2011; Tsugawa et al., 2011; Zettergren et al., 2017).

The rapid development over the past few decades of ground-based Global Navigation Satellite System (GNSS) receiver networks has allowed ionospheric responses to volcano-induced AGWs to be intermittently investigated based on sporadic eruption events. For instance, Roberts et al. (1982) found that ionospheric TIDs after the explosion of Mount St. Helens were detected 4900 km away with various propagation velocities between 350 and 550 m/s. Liu et al. (1982) found that some atmospheric perturbations for this same event were capable of traveling globally in the form of Lamb waves. Moreover, Heki (2006) observed that ionospheric total electron content (TEC) disturbances triggered by acoustic waves after the Asamo volcano eruption could propagate as fast as 1.1 km/s. Dautermann, Calais, and Mattioli (2009) and Dautermann, Calais, Lognonné, and Mattioli (2009) found that quasiperiodic TEC oscillations around 4 mHz were detected 18 min after the Soufrière Hill Volcano explosion and lasted 40 min, with various horizontal velocities between 500 and 700 m/s Shults et al. (2016) observed that the propagation velocity of ionospheric TEC disturbances after the Calbuco volcano eruption was around 900–1200 m/s, close to acoustic speeds at ionospheric heights. Nakashima et al. (2016) found that harmonic acoustic oscillations created by the Kelud volcano eruption lasted for 2.5 hr with ionosphere disturbances traveling at 800 m/s. These studies in aggregate have greatly informed community knowledge of co-volcanic ionospheric disturbances.

The recent Hunga Tonga-Hunga Ha'apai (herein simplified as Tonga) volcano eruption at 04:14:45 UT on 15 January 2022 was the largest eruption in the last three decades, causing significant wave perturbations from the ocean surface to the whole atmosphere across the globe in less than 24 hr (Duncombe, 2022). This event provides a unique scientific opportunity to advance the current understanding of volcano-induced local and global ionospheric responses. So far, prompt studies have provided some initial analyses of ionospheric disturbances after the eruption. For example, Themens et al. (2022) analyzed regional and global large-scale and medium-scale TID features following the eruption; Zhang et al. (2022) found global propagation of Lamb waves for three full cycles within 4 days; Lin et al. (2022) reported rapid appearance of disturbances in the conjugate Hemisphere; Harding et al. (2022) and Aa et al. (2022) found that strong horizontal neutral wind perturbations due to volcano eruption could considerably modify the equatorial electric field.

Despite these important early results, more features of this event remain to be analyzed. In this study, we use ground-based GNSS TEC data, satellite in situ measurements from Swarm and ICON, and ionosonde measurements to investigate two new phenomena associated with the Tonga volcano eruption: (a) A significant ionospheric plasma hole was observed near the eruption epicenter with a depletion magnitude of more than 10 TECU and a horizontal radius of 10–15°. (b) Pronounced post-volcanic evening equatorial plasma bubbles (EPBs) were continuously observed across a wide Asia-Oceania area of ∼140° longitudes following the arrival of Lamb waves, with magnitude decreased by 2–3 orders and lasted around 12 hr. In particular, this is the first time such dramatic plasma density depletion associated with volcano-induced AGWs has been reported. Our study also uses Beidou Geostationary Orbit (GEO) data for precise TEC measurements at stationary ionosphere pierce points (IPPs) near Tonga and accurate analysis of local ionospheric disturbances. These results are discussed in the following sections.

2. Instruments and Data Description

Ground-based GNSS TEC data are produced at the Massachusetts Institute of Technology's Haystack Observatory using 5000+ worldwide GNSS receivers, and are provided through the Madrigal distributed data system (Rideout & Coster, 2006; Vierinen et al., 2016). Besides traditional GPS/GLONASS TEC, we also used TEC from 240+ available Beidou receivers, especially from Beidou GEO receivers adjacent to eruption. Beidou GEO TEC data can provide more robust estimation from stationary IPPs in a manner less impacted by complicated ionospheric spatiotemporal variability. In addition to the absolute TEC, we also used two other quantities to investigate the ionospheric response to the eruption: (a) Detrended TEC (dTEC), characterizing the

wave-like ionospheric oscillations by removing a background variation trend for all satellite-receiver TEC pairs. Detrending is performed using a Savitzky-Golay low-pass filter with a 30-min sliding window (Savitzky & Golay, 1964; Zhang et al., 2017, 2019). (b) Rate of TEC Index (ROTI), describing dynamic ionospheric changes due to plasma irregularities and/or gradients. ROTI is defined as the 5-min standard deviation of the TEC time derivative (Aa et al., 2019; Cherniak et al., 2014; Pi et al., 1997).

Besides ground-based GNSS TEC, we also used in situ electron density (N_e) measurements from the European Space Agency's Swarm constellations (Friis-Christensen et al., 2008; Spicher et al., 2015). Swarm includes three identical satellites that fly in approximately circular orbits at 88° inclination. Swarm A and C fly side-by-side at around 450 km with 1.4° longitudinal separation, and Swarm B flies at around 510 km (Knudsen et al., 2017).

ICON is a low-Earth orbit satellite for ionospheric and thermospheric measurements that flies at an altitude of 575 km with an inclination angle of 27° (Immel et al., 2018). ICON carries Ion Velocity Meter (IVM) instruments that consist of the Retarding Potential Analyzer (RPA) and the Drift Meter (DM), which collectively provide ion density, the major ion composition, the ion temperature, and the ion velocity measurements (Heelis et al., 2017). In this study, we use ICON-IVM ion density and velocity measurements to analyze volcano-related ionospheric disturbances.

Moreover, the infrared brightness cloud temperature data, derived from Geosynchronous Operational Environmental Satellites (GOES) and other selected geostationary satellites (Janowiak et al., 2017), were also used to gauge volcano-related convection activity. Equatorial ionosonde measurements of F2-layer peak height (hmF2) and electron density profiles at GUAM (13.62°N, 144.86°E) are also utilized.

3. Results

3.1. Local Ionospheric Disturbances

Figure 1a shows the volcano epicenter location (20.5°S, 175.4°W) and the great-circle distances from the epicenter at an ionospheric height of 300 km. Also shown are four adjacent Beidou GEO receivers within 1000 km radius: TONG (21.02°S, 175.18°W), LAUT (17.5°S, 177.45°E), SAMO (13.76°S, 171.74°W), and FTNA (14.22°S, 178.12°W). Figure 1b shows a regional view with overlaid infrared brightness cloud temperature at 05 UT on 15 January 2022. The dark blue region over Tonga indicates a newly formed cold area with cloud temperature below 220 K. This was about 80–100 K lower than 1 hr ago, which indicates that the initial ash plume had protruded rapidly into the tropopause in less than 45 min triggering considerable atmospheric cooling. Also shown are fixed IPPs locations of Beidou GEO satellites C01 and C04 for each receiver.

The unique Beidou GEO observations with stationary IPPs allow us to accurately determine localized temporal ionospheric variations following the eruption (Figures 1c–1f). At TONG, the nearest station to the epicenter, after a minor increase following the eruption, the TEC curves showed three major cascading dips as marked by yellow shades. Collectively these formed an integrated depletion hole around 05 UT with a depletion amplitude of around 10 TECU. Smaller-scale periodic oscillations were also detected to embed in the depletion. Similar to TONG, LAUT TEC curves also exhibited three consecutive dips shortly after the eruption, with a clear phase and time delay between C01 and C04 among TONG and LAUT. Since fixed IPP locations from TONG and LAUT (corresponding to C01 and C04) were approximately arrayed radially outward in the same direction away from the epicenter (Figure 1b), we can collectively utilize their distance and phase/time information to deduce wave propagation parameters in this localized region. For SAMO and FTNA, the radial distances of their GEO IPPs were close, which made accurate detection of oscillation phase and time delay a little bit difficult compared to TONG and LAUT. Nevertheless, immense depletion features can also be seen at SAMO and FTNA through cliff-like TEC drops as large as 10–15 TECU, and were particularly prominent over SAMO around 5 UT. This volcano-induced effect was much earlier before local sunset around 0620–0700 UT, To further extract wave-like oscillations embedded in the depletion, Figure 1g plots all detrended Beidou GEO TEC curves in UT-distance coordinates. Volcano-induced fluctuations were generally within 0.5–3 TECU but sometimes reached 6 TECU. Recall from above that the TEC curves at TONG and LAUT showed three cascading dips as marked by yellow shades, thus the propagating velocities can be estimated using dTEC through slanted fiducial lines to connect iso-phase points at the valley for each dip from the same static IPP C01 and C04 between TONG and LAUT. The radial propagation velocity corresponding to these three major dips were calculated to be 760 m/s, 470 m/s, and 315 m/s, respectively. Specifically, taking the 315 m/s fiducial line as an example, we used detrended Beidou

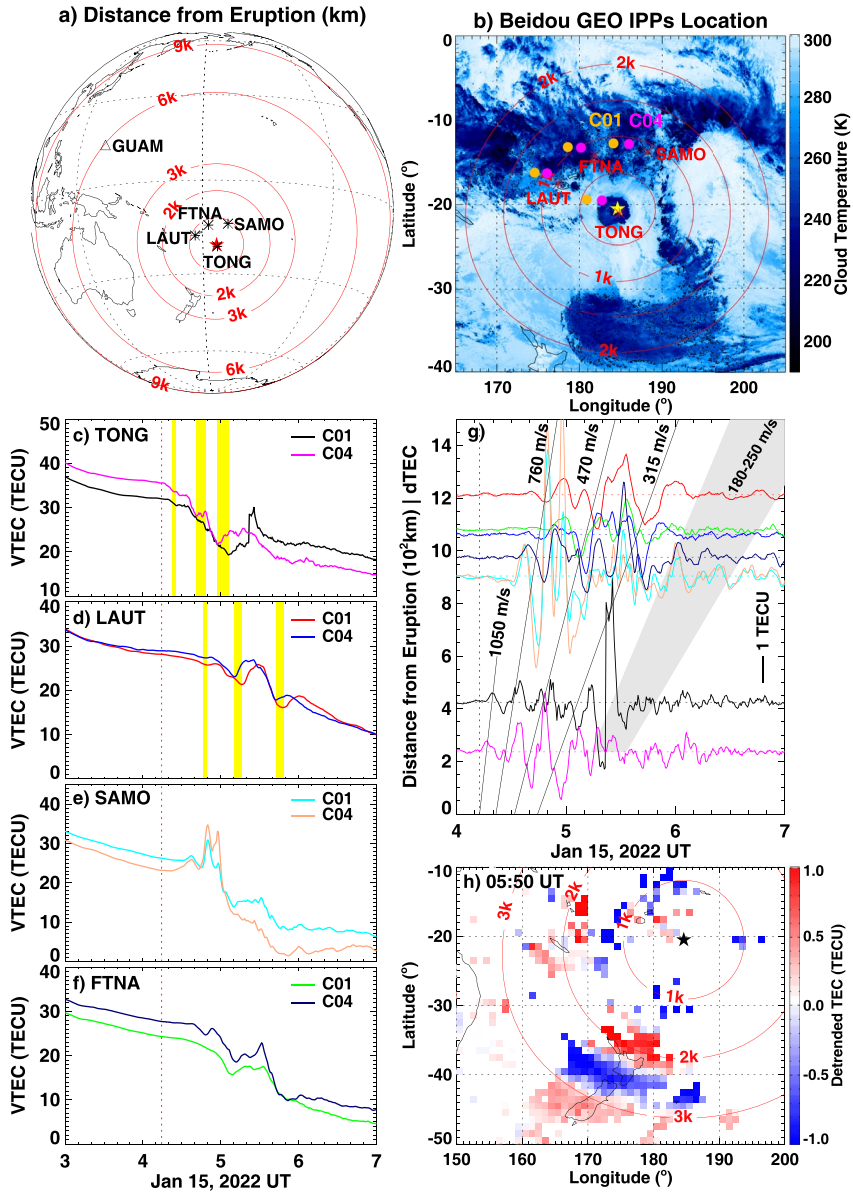

Figure 1. (a) Global view of the Tonga volcano eruption location (star), four adjacent Beidou geostationary orbit (GEO) receivers (asterisks), and an ionosonde (triangle). The iso-distance circles from the eruption epicenter are shown in red lines. (b) Regional view of above-mentioned information and corresponding Beidou GEO ionosphere pierce points location for C01 and C04 satellites, overlaid with the deep cloud brightness temperature observations at 05 UT on 15 January 2022. (c–f) Temporal variation of Beidou GEO total electron content (TEC) at four sites. The eruption time is marked by a vertical dotted line. Yellow shades mark three distinct TEC dips using TONG and LAUT measurements as examples. (g) UT-distance variation of detrended Beidou GEO TEC. The vertical line indicates eruption beginning time; the slanted lines and shades indicate different propagation velocities. (h) Observation of concentric traveling ionospheric disturbances near New Zealand using a two-dimensional detrended TEC map.

GEO TEC to search the time point when C01 TEC at TONG (black curve) and C01 TEC at LAUT (red curve) reached their respective local minimum point within the third major dip: 05:06:30 UT and 05:48:00 UT. Thus the propagation velocity in this region can be calculated using their IPP distance and time difference information, which was estimated to be 316.4 m/s. Similarly, when C04 satellite was used for the calculation, the estimated propagation velocity was 312.5 m/s. Taken as a whole, the fiducial line was estimated to be ~315 m/s. Moreover, some smaller-scale oscillations with velocities of 180–250 m/s were registered after major perturbations. If considering TONG measurements alone, another fast-traveling wave mode with 1050 m/s speed can be derived

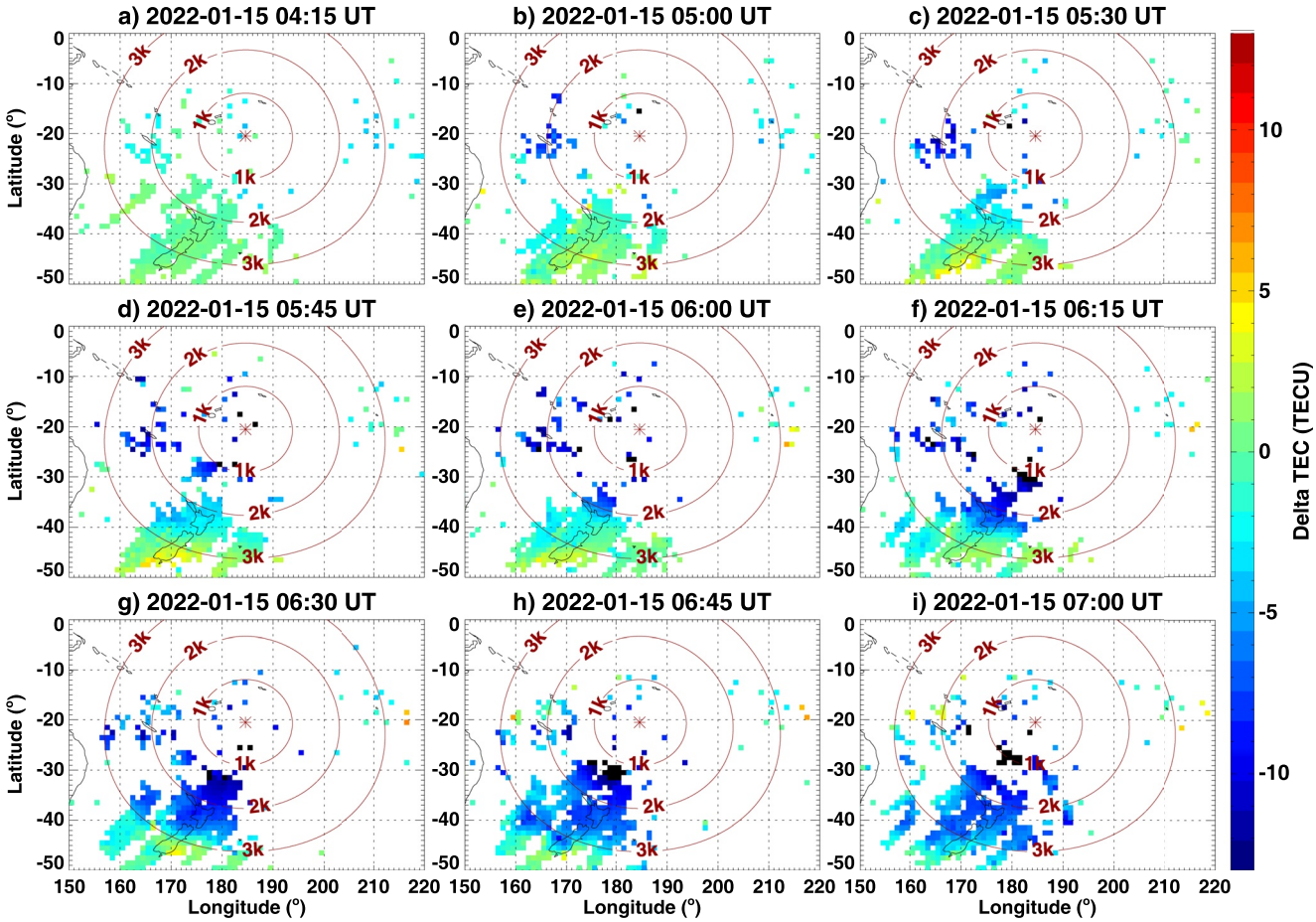

Figure 2. (a–i) Regional two-dimensional delta total electron content maps in the vicinity of volcanic eruption between 04:15–07:00 UT on January 15. The iso-distance lines from the eruption epicenter (asterisk) are shown in red circles.

by connecting two initial dTEC bumps at C01 and C04, though this fast wave did not seem to propagate beyond 1000 km.

We here mainly use TONG and LAUT to derive the fiducial lines since their corresponding IPPs are approximately radial outward aligned with respect to the eruption epicenter. There are some modest variations if using other pairs to do the calculation, say using TONG and SAMO, possibly due to their respective IPP points and epicenter are not aligned in a line, considering that the wave propagation could be un-isotropic in different direction. Despite fewer Beidou GEO observations as compared to GPS, these estimations have the key quality of being free from possible spatiotemporal variation contamination associated with normal moving IPPs. The estimated onset times of these continuous perturbations are marked in the horizontal axis of Figure 1g, which are similar to those derived in Astafyeva et al. (2022) using TONG-FTNA station pairs with multi-GNSS measurements. In addition, within the eruption near-field, Figure 1h displays a 2-D dTEC map combining multi-GNSS measurements to show concentric TID features over New Zealand at 2000–3000 km distance with an estimated wavelength of 1200–1500 km. These characteristics are generally consistent with recent studies (e.g., Themens et al., 2022; Zhang et al., 2022) and will not be described further in this study.

The local ionospheric hole of TEC depletion in the vicinity of the eruption center can also be observed in 2-D delta TEC maps at different time steps between 04:15–07:00 UT on January 15 as shown in Figure 2. The delta TEC values were calculated by subtracting averaged TEC values of three geomagnetically quiet reference days (January 11–13) before the volcano eruption. Despite some data gaps near the epicenter, the delta TEC results clearly demonstrated the evolution of local depletion structures. The signature of ionospheric hole can be seen around 05 UT near epicenter with sporadic points of TEC depletion for 5–10 TECU. This depletion continued

for at least two hours and extended outward forming a huge ionospheric hole with its magnitude reaching more than 10 TECU even around 2000 km away (Figures 2f–2h). The horizontal scale and magnitude of such a huge ionospheric hole is quite unique and impressive, which are much stronger than that of the famous Tohoku Earthquake-induced local ionospheric hole with 5–6 TECU depletion and horizontal size of 500 km (e.g., Saito et al., 2011; Tsugawa et al., 2011). The mechanisms of this local ionospheric hole will be further discussed in Section 4.

3.2. Global Ionospheric Disturbances With Strong EPBs

Besides significant local depletion, ionospheric ripples also propagated globally. Figures 3a and 3b show two examples of 2-D global ROTI maps on 15 January 2022 derived from 5000+ multi-GNSS receivers. At 12:00 UT, large ROTI values manifesting strong ionospheric irregularities were widely registered in the low and midlatitude East Asian sector around 6000–9000 km distance. At 14:00 UT, beside the Asian sector, noticeable gradients features were simultaneously found both in the North and South American area approximately parallel to the 12,000 km iso-distance line therein. To zoom in the propagation feature, Figures 3c–3h display six consecutive ROTI maps over the North American sector between 13:30–16:00 UT. The wavefront propagation signatures can be clearly seen via eastward structure movement in higher-than-background ROTI values that approximately parallel to iso-distance lines, which were marked with red arrows. The wavefronts propagated outbound from ∼11,000 km to ∼14,000 km with an average velocity of 315 m/s, consistent with one propagation mode in Beidou TEC results (Figure 1g). The full animation of the global ROTI variation is attached in Movie S1.

For widespread irregularity features in the Asian sector, Figures 3i–3n show six ROTI maps therein between 11 and 16 UT. Ionospheric irregularities were quite noticeable around the equatorial ionization anomaly (EIA) crests, which extended westbound from Indonesia, Philippines, and the Japan archipelago around 11:00 UT all the way to India and the Bay of Bengal around 15–16 UT. Moreover, to provide a global synoptic view with extended spatial/temporal ROTI coverage and to utilize space-borne observations, Figures 4a–4h show 16 consecutive paths of Swarm C (blue) and Swarm B (red) satellites that flew in the premidnight local time sector of 23 LT over Asia-Oceania area, overlaying on top of eight background ROTI maps between 08:30–19:30 UT on January 15. The iso-distance lines away from the eruption epicenter are shown by black circles with the anticipated wavefront of Lamb waves being marked by a green circle. The right panels in each subfigure display the corresponding geomagnetic latitudinal profiles of in situ N_e for Swarm C (even number) and Swarm B (odd number) paths, respectively. The reference background N_e profiles from the day before (dotted lines) and after (dashed lines) were also plotted for comparison. The westbound phase extension of locally developed plasma irregularity features shown by high ROTI values is generally in concert with the anticipated Lamb waves propagation. Moreover, the volcano-induced local and global ionospheric disturbances can also be derived from Swarm plasma density profiles. At 08:30 UT (Figure 4a), Swarm B and C were flying on the eastern side of the volcanic eruption epicenter about 30–40° longitude away, which did not detect considerable plasma irregularities. At 10 UT (Figure 4b), Swarm C was flying around 167.8°W longitude, merely 7–8° from that of the volcanic eruption. A broad equatorial plasma depletion with a latitudinal width of 20–25° was registered in Swarm C Path 02 comprising of smaller-scale plasma irregularities, in which the plasma density was reduced by 2–3 orders of magnitude reaching as low as 10^2 cm^{-3}. Such a broad equatorial plasma depletion suggests that the equatorial ionospheric height was significantly uplifted near the volcanic eruption longitude possibly by an enhanced fountain effect, so that the satellite might fly below the F2-region peak height while crossing the equatorial region to encounter a low-density trough (Kil & Lee, 2013; Lee et al., 2014). At 11:30 UT (Figure 4c), Swarm C and B were flying across the western side of volcanic eruption around 168.8°E and 179.2°E longitudes, respectively. As can be seen, significant equatorial and low-latitude plasma bite-outs with the density as low as 10^2–10^3 cm^{-3} were quite obvious in both profiles, which were 2–3 orders of magnitude lower than reference levels. The irregularity activity on reference days is much weaker. Besides noticeable plasma bubbles, a significant feature of the local ionospheric hole was also registered in Swarm B profile of Path 03 between 20 and 40°S geomagnetic latitude, thus the latitudinal radius of the ionospheric hole was estimated to be ∼10° that consistent with TEC measurements in Figure 2. In the following time steps, similar signatures of strong plasma bubbles can also be consecutively observed by Swarm satellites across Papua New Guinea (Figure 4d), East Asia (Figure 4e), Indonesia (Figure 4f), India (Figure 4g), and even partially east African sector (Figure 4h). These ground-based GNSS ROTI and space-borne in situ N_e data collectively indicate that strong post-volcanic EPBs continuously developed

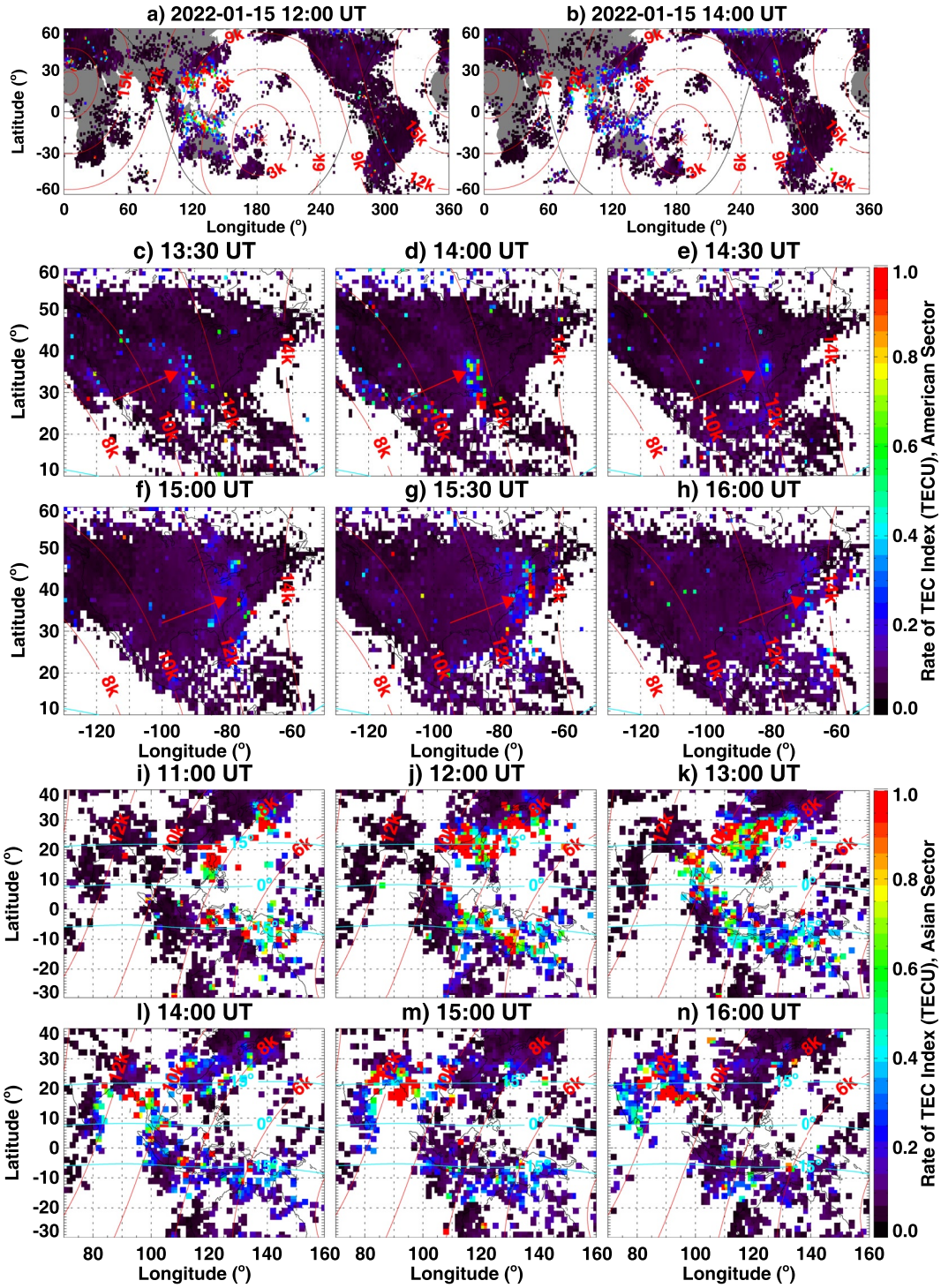

Figure 3. (a and b) Global 2-D Rate of total electron content Index (ROTI) maps at 12 UT and 14 UT on January 15. The volcano eruption location (asterisk), iso-distance lines from eruption (red lines), and solar terminator (black line) are marked (c–h) Regional ROTI maps over North America between 13:30–16:00 UT. The red arrows mark the propagation of volcano-induced wavefront. (i–n) Regional ROTI maps over Asian sectors between 11 and 16 UT. The iso-distance lines from eruption (red lines) and the geomagnetic equator and ±15° lines (cyan) are marked.

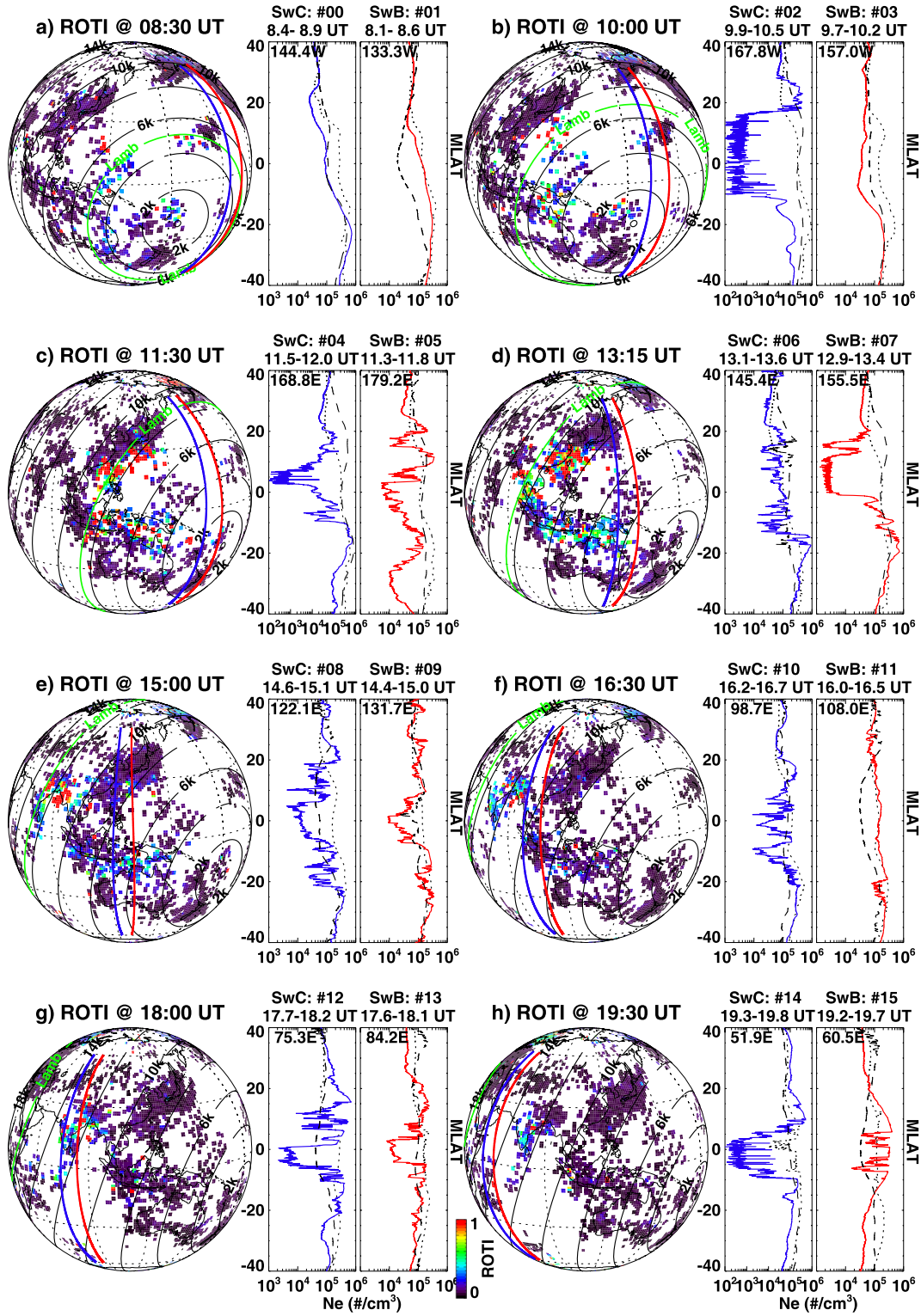

Figure 4. (a–h) Global Rate of total electron content Index maps focusing on Asia-Oceania sector at eight time steps between 08:30–19:30 UT on 15 January 2022 with overlapping Swarm C (blue) and Swarm B (red) paths. The iso-distance lines from eruption are marked with black circles. A green circle marks the anticipated wavefront propagation of atmospheric Lamb waves. The right two panels in each sub-figure show corresponding electron density variation as a function of geomagnetic latitudes along Swarm paths around 23 LT. The paths are marked with even (odd) numbers for Swarm C (B). The black dotted and dashed lines show corresponding reference profiles from the day before and after the volcano eruption, respectively.

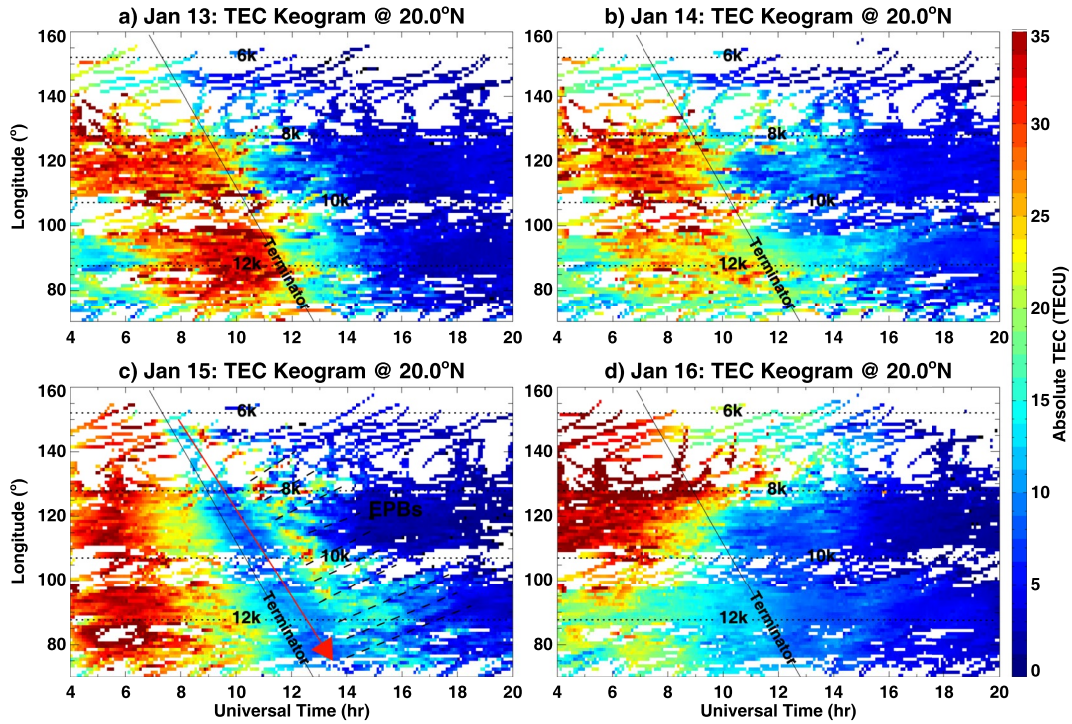

Figure 5. (a–d) Total electron content (TEC) keograms as a function of time and longitude along 20° latitude during January 13–16, respectively. The terminator (solid lines) and iso-distance lines (dotted) from volcano eruption are also shown. The red arrow in Figure 5c marks a significant TEC erosion following the anticipated Lamb wave passage. Quasi-parallel dashed lines in Figure 5c mark quasi-periodic equatorial plasma bubbles that embedded within the equatorial ionization anomaly crest.

across a wide Asian sector covering more than 140° longitudes at local postsunset period on January 15. This is reported for the first time after an extreme volcano eruption.

The latitudinal/altitudinal extension of these post-volcanic EPBs is also worth discussing. In particular, Swarm profiles in Figure 4e showed that EPBs likely extended to ±20–25° geomagnetic latitudes (MLAT) in the East Asian sector, indicating that the Apex height of these EPBs may reach ∼1500 km above the equator. This is quite similar to those shown in Shiokawa et al. (2004), suggesting a large upward plasma drift speed in the equatorial region. Similar high-altitude EPBs were occasionally observed in the literature. For example, Ma and Maruyama (2006) found that EPBs could be observed at 31° MLAT in GNSS TEC observations; Foster and Rich (1998) reported that EPB signatures could be observed by Millstone Hill incoherent scatter radar at 35–37° MLAT; Katamzi-Joseph et al. (2017) and Cherniak and Zakharenkova (2016) reported that EPBs can extend to 40° MLAT in Europe using ground-based TEC and in situ measurements (Aa et al., 2019). found that bubble-like ionospheric depletion structures could expand to much higher latitudes of 46°MLAT that map to Apex height of more than 6000 km. In contrast, the latitude/altitude extension of these post-volcanic EPBs reported in this study is smaller than and different from those storm-induced super plasma bubbles.

To better investigate the EPBs' evolution and their connection to volcano-induced waves, Figures 5a–5d show original TEC keograms as a function of time and longitude along 20°N (the approximate latitudinal location of northern EIA crest over the Asian sector) during January 13–16, respectively. The EIA crest morphology on January 15 (Figure 5c) was considerably different from the other reference days with more natural variation. In particular, the EIA crest intensity on January 15 was significantly eroded by more than 10 TEC unit between 09 and 14 UT, with a sharp edge following the consecutive passage of dusk terminator and anticipated westward-propagating Lamb wave from 6,000 km to 12,000 km that marked by a red arrow. The disturbance propagating speed was estimated to be 310–350 m/s that consistent with the estimated atmospheric Lamb wave velocity from recent studies (Themens et al., 2022; Zhang et al., 2022). Most importantly, shortly after the passage of disturbed TEC depletion, noticeable low-density dark streaks representing EPBs with comb-like periodic longitudinal distribution (shown by quasi-parallel black dashed lines) were developed and embedded within the partially recovered

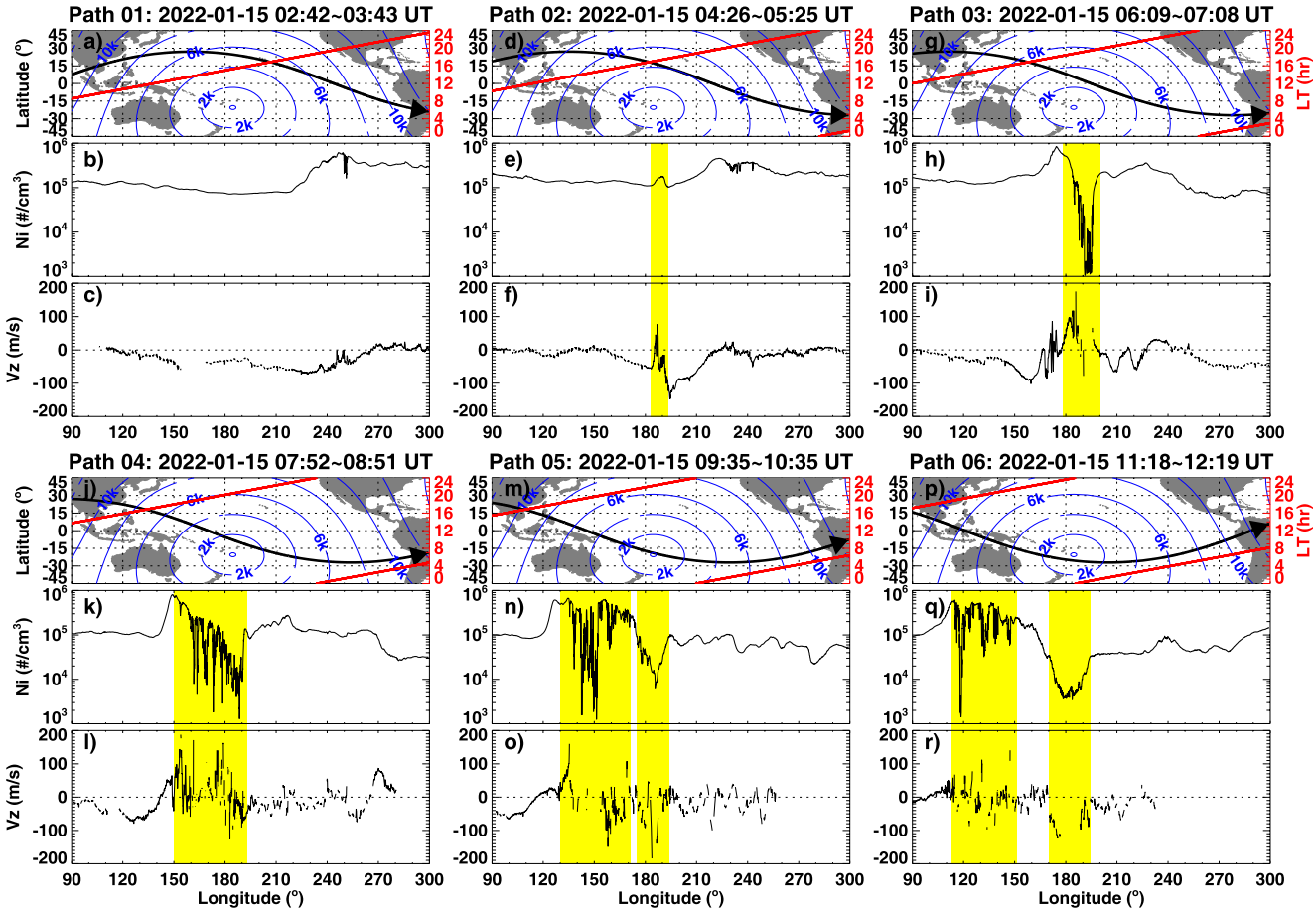

Figure 6. (a–r) ICON-IVM observation tracks and corresponding local time, ion density, and vertical drift results for six consecutive paths between 02:42–12:19 UT on 15 January 2022. Iso-distance lines away from the Tonga volcano eruption epicenter with 2000 km interval are also marked on maps. The shaded regions mark noticeable plasma density and/or drift disturbances after the volcano eruption.

EIA crest. The inter-bubble distance was estimated to be around 400–900 km, similar to those indicated in previous studies on periodic EPBs structures (e.g., Aa, Zou, Eastes, et al., 2020; Das et al., 2020; Huba & Liu, 2020; Makela et al., 2010; Takahashi et al., 2015). These notable features of EIA bite-out and periodic EPBs after the passage of Lamb waves provide important evidence of the novel linkage between volcano eruption and ionospheric disturbances, which will be further discussed in the next section.

ICON-IVM in situ measurements also observed significant co-volcanic and post-volcanic ionospheric disturbances. Figure 6 shows ICON-IVM observation tracks and corresponding local time, ion density, and vertical drift results for six consecutive paths between 02:42–12:19 UT on 15 January 2022. In Path 01, the plasma density and vertical drift variation were generally smooth over the Asia-Oceania sector with merely small fluctuations before the Tonga volcanic eruption. Starting from Path 02, however, significant plasma density and drift disturbances were registered following the volcanic eruption around the epicenter and adjacent area. For example, at ~04:55 UT in path 02, both plasma density (Figure 6e) and vertical drift (Figure 6f) exhibited a sudden bump of "plasma blob" near the volcanic eruption longitude around 185° (175°W), although the latitudinal location of ICON observation was in the conjugate northern hemisphere at this moment around 4,000 km away from the epicenter. This would either require a fast propagation mode (e.g., Rayleigh wave) of ~1700–1800 m/s that much larger than those known air pressure acoustic wave modes indicated in Themens et al. (2022) and Zhang et al. (2022); or an alternative explanation, as suggested by Lin et al. (2022) and also implied from the vertical plasma drift spike, is that this was more like a conjugate disturbance signature due to instantaneous magnetic field mapping effect of polarization electric field induced by significant zonal wind perturbation due to volcano-induced AGWs. Future

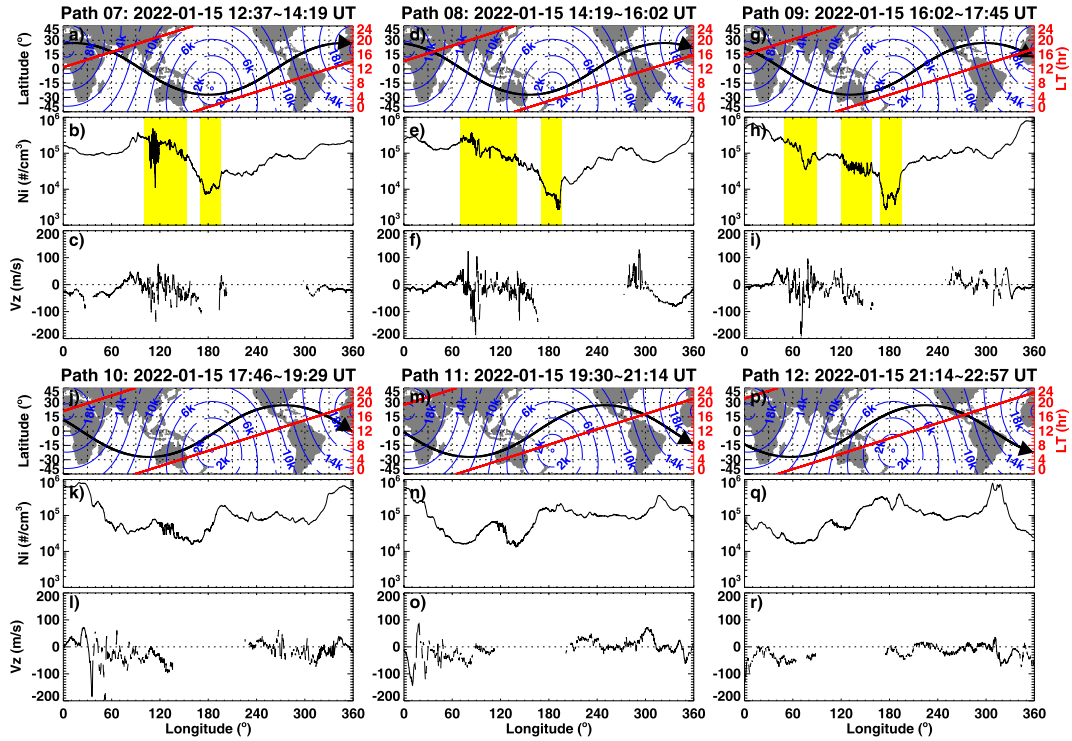

Figure 7. (a–r) The same as Figure 6, but for six following paths of ICON-IVM between 12:37–22:57 UT on 15 January 2022.

modeling effort and data analysis is still needed to further verify the exact mechanism of this fast conjugate response, which is beyond the scope of the current paper.

The most striking features shown by ICON-IVM are the strong plasma trough embedded with plasma bubbles that appeared starting from Path 03. In particular, when ICON was crossing the volcano eruption longitude between 180 and 195°E around 06:40 UT (Figures 6h, 19 LT), the in situ plasma density experienced a drastic depletion of two orders of magnitude, reaching as low as 10^3 cm^{-3} that highlighted by yellow shades. Moreover, noticeable EPBs were embedded within this huge equatorial plasma trough and were associated with large vertical E × B drift of 60–120 m/s (Figure 6i), representing enhanced fountain effect near the local dusk after the volcanic eruption, which was favorable for the amplification of Rayleigh-Taylor instability growth rate and development of plasma irregularities (Kelley et al., 1976). Similarly, in Path 04, strong postsunset EPBs with 1–2 orders of magnitude depletion and large vertical E × B drift of 60–120 m/s extended westward between 150 and 190° longitudes around 08:15 UT. Moreover, in the following two paths, the deep local plasma hole remained nearly stationary around the eruption center. At the same time, significant postsunset EPBs in the Asian sector were gradually separated from the local plasma hole but continuously developed at further westward longitudes across 130–170°E around 10:00 UT in Path 05 and about 110–150°E around 11:40 UT in Path 06. Two important results can be derived from these observations: (a) the horizontal size of the local plasma hole was quite noticeable, with an estimated radius of around 10–15° that consistent with the TEC results (Figure 2) and Swarm B estimation (Figure 4c); (b) the westward propagating phase speed of the continuously developed EPBs was estimated to be 310–350 m/s that generally agree with the Lamb waves velocity (Themens et al., 2022; Zhang et al., 2022).

Figure 7 displays similar ICON-IVM results for the following six orbital paths between 12:37–22:57 UT on January 15. Local plasma hole and strong EPBs were still quite considerable in Paths 07–09 as shown by yellow shades, which are consistent with Swarm results. Starting from Path 10, this long-lasting local plasma hole seemed to be filled possibly by sunrise photo-ionization, as ICON passed the volcanic eruption longitudes in the local morning. EPBs in the Asian sector were gradually diminished though still discernible to some extent. One thing to note is that such a deep local plasma hole and strong EPBs continued for more than 10 hr before completely subsidized, which is surprisingly unique and will be further discussed in the next section.

4. Discussion

4.1. Huge Local Ionospheric Plasma Hole and Oscillations

Beidou GEO TEC observing geometries provided a unique opportunity to continuously observe and precisely evaluate the volcano-induced local ionosphere characteristics using fixed IPPs. The most direct feature near the epicenter was a significant ionospheric hole with depletion magnitude of more than 10 TECU, formed by consecutive cliff-like TEC drops. Such a deep ionospheric hole was also observed in the 2-D delta TEC maps with 10+ TECU reduction and in ICON-IVM plasma density measurements with 1–2 orders of magnitude depletion. In particular, this ionospheric hole has a broad horizontal size with an estimated radius of 10–15° and continued for several hours. Surprisingly, such a huge depletion feature near the epicenter was registered in ICON-IVM plasma density profiles for more than 10 hr until local sunrise. Although a similar phenomenon of a transient co-seismic ionospheric "hole" near the epicenter has been occasionally reported before (e.g., Astafyeva et al., 2013; Kakinami et al., 2012; Tsugawa et al., 2011), the magnitude, size, and duration of such a huge ionospheric hole after this volcanic eruption are quite distinct. For example, the local depletion feature associated with the 2011 Japan Tohoku earthquake has a magnitude of 5–6 TECU reduction, a horizontal scale size of 500 km, and a duration of 60 min (Saito et al., 2011), which are considerably less than those of the Tonga volcanic eruption.

The underlying mechanism of such a huge plasma hole is still under debate. For example, Kakinami et al. (2012) suggested that this is a tsunami-related depletion induced by ionosphere descent and recombination enhancement through meter-scale sea surface downwelling at the tsunami source region. However, Kamogawa et al. (2015) indicated that this depletion could instead occur after a large inland earthquake. Astafyeva et al. (2013) demonstrated that the depletion represents the rarefaction phase of shock-acoustic waves following large inland or undersea earthquake. Moreover, numerical simulation results given by Shinagawa et al. (2013) and Zettergren et al. (2017) collectively indicated that the TEC depletion was likely caused by strong expansion and upwelling in the thermosphere along with outward ionospheric plasma flow driven by impulsive nonlinear shock-acoustic wave pulses. This latter mechanism helps explain our direct observational evidence in this Tonga event: the local TEC depletion was composed of cascading decreases that correspond to different shock-acoustic wave impulses. In addition, Astafyeva et al. (2022) also observed this plasma hole and indicated that the Tonga volcanic eruption from shallow underwater should generate stronger shock waves with large amplitude and prolonged rarefaction phase than those from an inland earthquake. This helps explain the unprecedented magnitude and size of the ionospheric hole. Another thing worth noting is that this local plasma hole was established near local dusk with a long-lasting duration that registered in ICON-IVM ion density profiles (Figures 6 and 7) for more than 10 hr until local sunrise, primarily due to shortage of nighttime photo-ionization source with low background density level, as well as lack of field-aligned plasmaspheric refilling due to smaller dip angle in the low-latitude region.

Besides the large ionospheric hole, several acoustic-gravity oscillation modes with different propagation velocities were identified. The fast modes with 1050 m/s and 760 m/s, arising from different excitation conditions, fall within the sound speed range at ionospheric heights and are comparable to prior studies (e.g., Calais et al., 1998; Heki, 2006; Heki & Ping, 2005; Otsuka et al., 2006). These modes are considered to be caused by acoustic pressure waves generated from the sea surface at the epicenter (Astafyeva, 2019; Chen et al., 2011; Tsugawa et al., 2011). The subsequent medium-speed modes between 300 and 500 m/s range could be associated with lower-frequency infrasonic and/or gravity parts of AGWs, which propagated to at least 3500 km away as deduced from Figure 1h. The ionospheric disturbances also included a slower propagation mode with speeds of 180–250 m/s, due to gravity waves triggered by volcano and/or tsunami–atmosphere–ionosphere coupling processes (e.g., Artru et al., 2005; Azeem et al., 2017; Huba et al., 2015; Meng et al., 2018; Savastano et al., 2017).

4.2. Strong Post-Volcanic EPBs

The most significant discovery of this study is the presence of strong and long-lasting post-volcanic EPBs that continuously developed across the Asia-Oceania area on January 15, covering a wide longitudinal range for more than 140° with duration ≥12 hr and N_e decrease of 2–3 orders of magnitude at Swarm/ICON altitude between 450 and 575 km. In contrast, EPB activities on the day before and after the volcano eruption were much weaker as shown in Figure 4. It is known that EPBs are large-scale plasma density depletions that usually form in the postsunset bottomside F region at the equatorial and low-latitude ionosphere, under favorable conditions of prereversal enhancement (PRE) and increased Rayleigh-Taylor instability growth rate with steep vertical density

gradients after the decay of E region (e.g., Aa et al., 2019; Abdu, 2005; Karan et al., 2020). Although co-seismic and co-volcanic AGWs and associated ionospheric oscillations have been widely reported, to the best of our knowledge, such widespread and long-lasting post-volcanic EPB features have never been reported before, especially considering that the seasonal behavior of EPBs' occurrence over Asian and Pacific sector is typically quite low around January that derived from climatology studies (e.g., Aa, Zou, & Liu, 2020; Burke et al., 2004; Kil et al., 2009). The mechanism of these anomalous post-volcanic EPBs needs detailed discussion.

The first thing to consider is magnetospheric driving forces from above since this volcano eruption happened during the recovery phase of a moderate geomagnetic storm. Depending on storm phases and local time sectors, the EPBs occurrence can be enhanced or inhibited primarily via modified equatorial electrodynamic effects caused by the penetration electric field (PEF) due to suddenly varying magnetospheric convection, and/or disturbance dynamo electric field (DDEF) due to changes in global thermosphere circulation. (a) Storm enhances EPBs. This usually occurs in the storm main phase when PEF has the same eastward polarity as dusktime PRE. This combination leads to increased upward equatorial plasma drift and the enhanced postsunset rise (PSSR) of F-layer height, which provides favorable conditions to enlarge the growth rate of Rayleigh-Taylor instability (e.g., Aa et al., 2019; Cherniak & Zakharenkova, 2016; Jin et al., 2018; Tulasi Ram et al., 2008). In some rare cases, nighttime DDEF can sometimes excite atypical predawn EPBs (Zakharenkova et al., 2019). (b) Storm inhibits EPBs. This usually occurs in the storm recovery phase when DDEF has been built up with a westward polarity in the daytime through local dusk. The modified westward equatorial zonal electric field leads to downward plasma drift and lowering of the F-layer, causing suppression of postsunset EPBs (e.g., Carter et al., 2016; Li et al., 2009).

For this event, Figures 8a–8e show temporal variation of interplanetary and geomagnetic parameters between January 13–16, 2022. On January 14, following a coronal mass ejection (CME) arrival, the IMF Bz (Figure 8b) rotated to a sustained negative direction after 15 UT, reaching a minimum value of −17 nT at 22:25 UT and quickly flipped northward. This indicates the existence of large PEF at the end of January 14 as also shown in IEF Ey (Figure 8c). The Kp index reached 6 between 21 and 24 UT and the longitudinally symmetric index (SYM-H) reached a minimum value of −100 nT at 22:25 UT, which registered this storm as a moderate storm. The large PEF existed around 16–23 UT on January 14, the previous day of the volcano eruption. During this period, the Asia-Oceania sector was rotating from local midnight to morning with westward PEF, which inhibited EPBs occurrence therein as can be seen from background dotted lines in Swarm N_e in Figure 4. However, we emphasize that the observed significant EPBs in the Asia-Oceania sector were mainly around 06–18 UT on January 15, about 12 hr after this large PEF. As can be seen, the IMF Bz and IEF has already subsided and exhibited merely small perturbations at least between 04 and 15 UT on January 15 before detected EPBs. Thus, it is hard to prove that the large PEF, which inhibited EPBs in the Asian-Oceania sector on January 14, would have continued for over 12 hr and caused resurgent EPBs on the second day, since the penetration effect is typically prompt and short-lived in a couple of hours. There were some fluctuations in IMF and IEF since 15 UT on January 15 due to the arrival of coronal hole high-speed stream, which may provide intermittent PEF to maintain plasma bubbles. However, the initial equatorial trough and plasma bubbles occurred much earlier around 06–07 UT as shown by ICON-IVM results. Moreover, January 16 also registered moderate IMF Bz and IEF Ey fluctuations in the latter half of the day, suggesting the existence of intermittent PEF similar to that of the volcano eruption day, yet the EPBs activity was much weaker on January 16 as can be seen from dashed lines in Figure 4. These collectively indicate that the intermittent PEF was unlikely the dominant driver of significant EPBs over the Asia-Oceania sector on volcano eruption day.

We next discuss the potential DDEF effect. The observed EPBs occurred in the storm recovery phase, and it is possible that DDEF may have been built up around low latitudes. However, it is known that the polarity of DDEF is typically westward in the daytime through local dusk (M. Blanc & Richmond, 1980), which normally causes storm-time inhibition of EPBs in the postsunset sector via downward E × B drift to reduce the instability growth rate (e.g., Carter et al., 2016; Li et al., 2009). In this study, significant EPBs occurred in the postsunset hours. Thus, we deduce that the storm-time DDEF is unlikely the primary cause of this event. Moreover, the ICON-IVM drift results in Figures 6f and 6i showed that the vertical plasma drift exhibited a sudden enhancement right around the eruption longitude. The storm-induced penetration or disturbance dynamo electric fields are not expected to have such a sharp longitudinal distinction but usually exhibit a wide longitudinal coverage with the same polarity during the day/night. Last but not least, recent studies given by Harding et al. (2022)

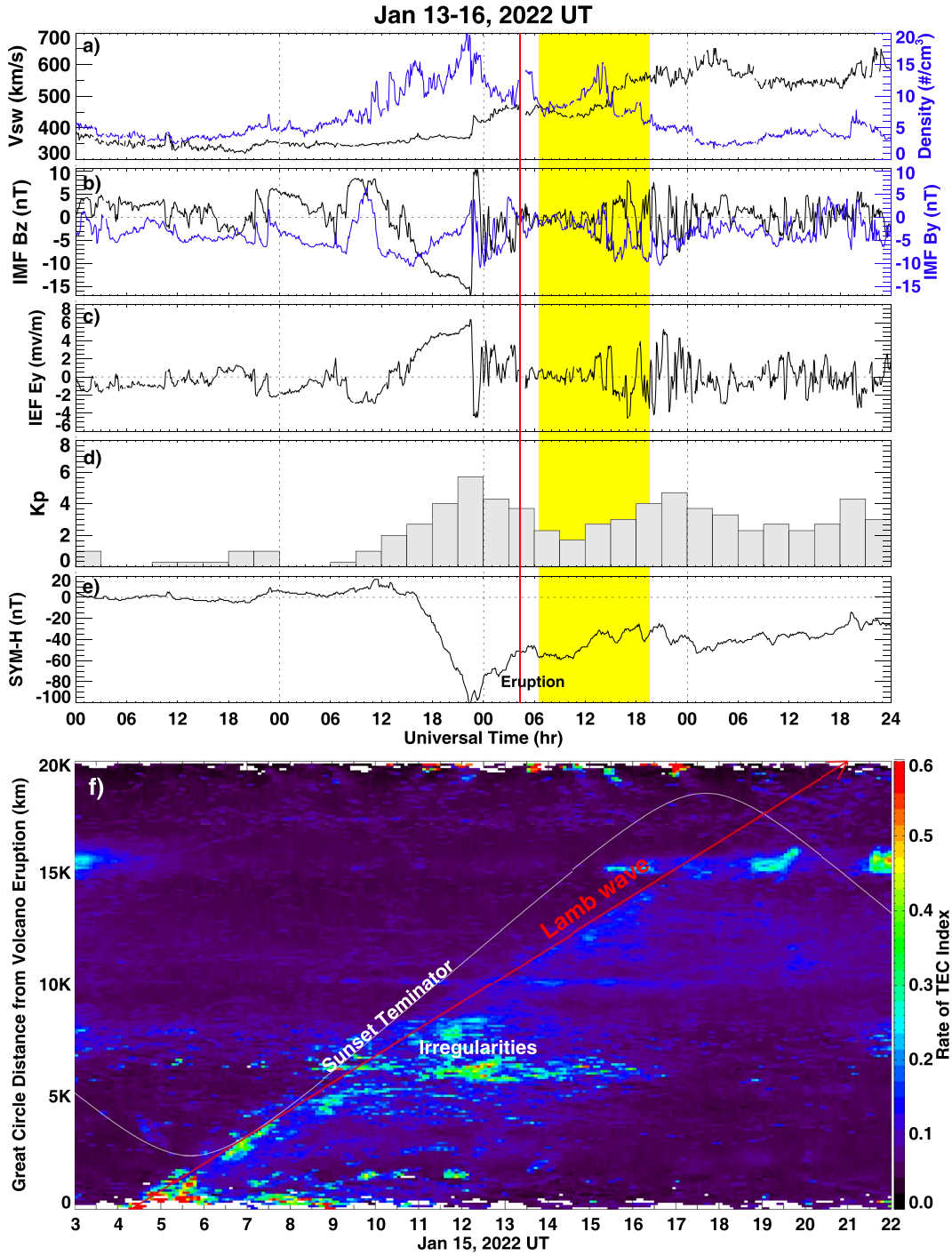

Figure 8. Temporal variation of (a) Solar wind speed and proton density, (b) Interplanetary magnetic field By and Bz, (c) interplanetary electric field By, (d) Kp index, and (e) Longitudinally symmetric index (SYM-H) during 13–16 January, 2022. The volcano eruption time was marked with a vertical red line. The yellow shade marks the approximate time period for equatorial plasma bubbles (EPBs) observations. (f) UT-distance variation of ROTI values. The Lamb wave propagation trend (red line) and equatorial sunset terminator (white line) was also marked.

and Le et al. (2022) have investigated equatorial electrojet activities for this same event using ICON/MIGHTI neutral wind measurements, Swarm field-line current data, and ground-based magnetometer data, indicating that the penetration and DDEF from this geomagnetic storm had minimal impact on the equatorial electric field perturbation.

Therefore, besides the storm effect, we next discuss lower atmosphere forces after the volcano eruption. Figure 8f shows a GNSS ROTI figure as a function of universal time and great-circle distance from volcano eruption location. This time-distance plot was constructed to compensate for the uneven GNSS data distribution by binning all available ROTI measurements in terms of the universal time and great-circle distance from the volcano eruption site. Note that high-latitude ROTI data above 65° geomagnetic latitude were excluded to eliminate space weather impacts as much as possible. This time-distance figure would allow us to better identify and trace the volcano-induced disturbances propagation signature. As can be seen, volcano-induced ionospheric disturbances traveled globally at least 16,000 km away from the epicenter. By calculating the slope of the fitted line along the discernible boundary, the global propagation velocity of ionospheric ROTI disturbances is about 315 ± 15 m/s, consistent with the globally propagating nature of less-attenuating atmospheric Lamb waves from historical and recent corroborations (Bretherton, 1969; Lindzen & Blake, 1972; Themens et al., 2022; Zhang et al., 2022). Despite Lamb waves are normally concentrated within a few scale heights in the troposphere/stratosphere, their energy can tunnel into the thermosphere via acoustic-gravity resonance at certain frequencies and thus can further cause ionospheric disturbances (Nishida et al., 2014). Thus, we observed moderate-to-high ROTI values (>0.25) representing strong ionospheric irregularities that predominantly occurred between 3000 and 10,000 km range around 07–16 UT, mainly contributed by Asia-Oceania observations, following the continuous passage of equatorial sunset terminator and volcano-induced Lamb waves.

This coincident terminator/wave passage and irregularities suggest that acoustic-gravity resonance and coupling with Lamb waves may explain the occurrence of such strong EPBs. It is known that the connection between gravity waves and plasma bubbles have been widely studied using both observations and numerical simulations. For example, Hysell et al. (1990) found gravity wave modulations were related to radar irregularity plume formation over Jicamarca; Rottger (1981) indicated that gravity waves from convective thunderstorms have a reasonable impact on equatorial spread-F irregularities; Singh et al. (1997) indicated that plasma bubble signatures can be developed from wavy ion density structures in the bottomside F layer; Takahashi et al. (2009) and Fritts et al. (2008) observed simultaneous appearance of periodic EPBs and upward propagating gravity waves reaching thermospheric height during the Spread F Experiment. Huang and Kelley (1996) simulated the non-linear evolution of Spread-F irregularities induced by the zonally propagating gravity waves. Numerical simulations given by Krall et al. (2013) and Tsunoda (2010) investigated the seeding role of Spread-F irregularity due to plane and circular gravity waves, respectively. Despite these interesting studies, our analysis of this unique natural hazard event indicates a novel linkage between the volcanic eruption and plasma bubbles that provides further evidence to help verify and understand the underlying mechanisms.

In particular, the development of plasma bubbles could be attributed to volcano-induced AGWs via the following three mechanisms:

4.2.1. Direct Seeding Mechanism

The wave disturbances propagating upward at slant angles could produce needed perturbation winds, providing precursor modulations in the electron density and/or polarization electric field to initiate the instability growth (e.g., Huang & Kelley, 1996; Krall et al., 2013; Huba & Liu, 2020; Retterer & Roddy, 2014; Tsunoda, 2010). In particular, the meridional wind perturbations of gravity waves could produce plasma density modulations via dynamic effect; the zonal and vertical wind perturbations across geomagnetic field lines can generate polarization electric field (Abdu et al., 2009). Both of which contribute to the instability growth of EPBs development. Using ICON thermospheric wind measurements, Harding et al. (2022) and Aa et al. (2022) found that both zonal and meridional winds exhibited strong oscillations as large as ±200 m/s following the passage of volcano-induced Lamb waves. This could provide initial seed perturbations that lead to the development of EPBs.

4.2.2. Destabilize Bottomside Ionospheric Gradient

The gravity wave amplitude is known to increase exponentially with respect to altitude due to decreasing atmospheric density, which could form large-scale wave structures in the bottomside F region that undulate F layer heights to elevate and destabilize bottomside density gradients (Abdu et al., 2009; Tsunoda et al., 2011). Several studies have thus indicated that EPBs could be developed at the crests of large-scale wave structures and exhibited periodic longitudinal distributions with inter-bubble distances of several hundred kilometers (e.g., Aa, Zou, Eastes, et al., 2020; Das et al., 2020; Makela et al., 2010; Takahashi et al., 2015). For this volcanic eruption event, the observed EPBs also exhibited quasi-periodic longitudinal structures as shown in TEC keogram (Figure 4c)

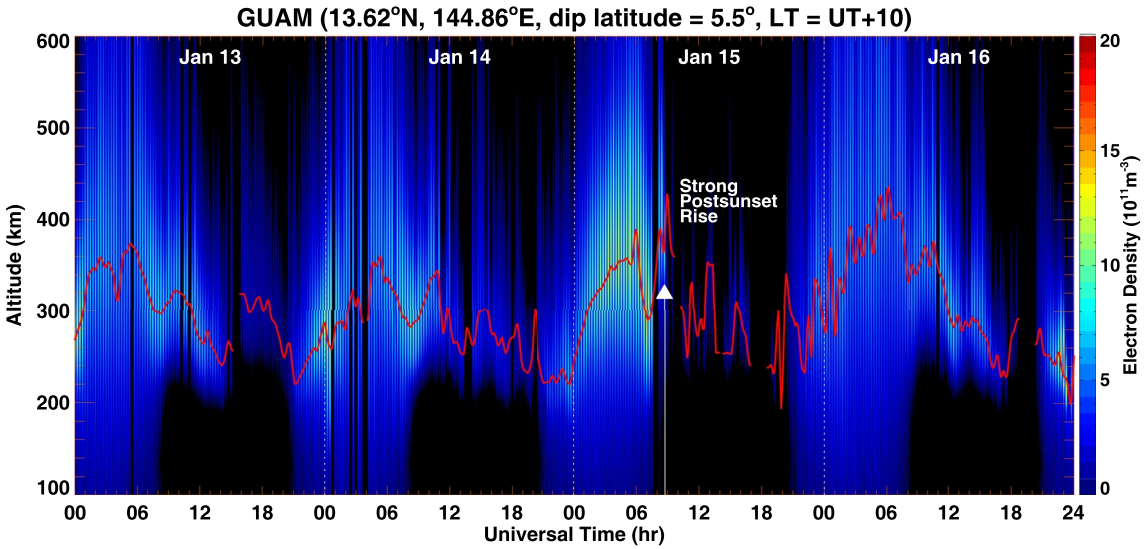

Figure 9. GUAM ionosonde measurements of electron density profiles and F2-layer peak height (hmF2) during 13–16 January, 2022. The white arrow marks the anticipated arrival time of atmospheric Lamb waves that were associated with strong postsunet rise of equatorial F layer around 09 UT on 15 January.

and in ICON-IVM plasma density profiles (Figures 6k, 6n, and 6q), which are consistent with the horizontal wavelength of several hundred kilometers for the global propagating TIDs related to Lamb waves in both near-field and far-field (Zhang et al., 2022). This further demonstrates the existence and influence of Lamb wave-induced gravity waves in triggering EPBs.

4.2.3. Enhancement of PRE and Postsunset Rise of Equatorial F-Layer

Gravity waves can be a necessary factor to trigger initial plasma perturbations but may not always be a sufficient source leading to plasma bubbles (Huba & Liu, 2020). The background ionospheric condition, especially the equatorial vertical E × B drift, is a key factor that directly influences the Rayleigh-Taylor instability growth rate (Sultan, 1996). It is known that large eastward thermospheric wind near the equatorial dusk region is responsible for the PRE via the F-region dynamo effect (Eccles et al., 2015; Rishbeth, 1971). The PRE peak intensity could be enhanced by in-phase superposition of eastward perturbation wind due to AGWs and the background zonal wind (Abdu et al., 2009; Kudeki et al., 2007). Some recent studies showed that this volcanic eruption caused extreme thermospheric zonal winds oscillation with the maximum eastward component reaching 200 m/s together with strong equatorial electrojet following the passage of volcano-induced Lamb waves (Harding et al., 2022; Le et al., 2022). In comparison, our study of the ICON-IVM vertical drift measurements clearly demonstrates that the dusktime PRE near epicenter longitude was indeed largely enhanced to 60–120 m/s (Figures 6f, 6i, and 6l) following the volcanic eruption. Moreover, the broad equatorial plasma depletion with 20–25° latitudinal width in Swarm B Ne profile of Path 02 (Figure 4b) also implied that the ionospheric height near the epicenter longitude could be significantly uplifted so that satellite was likely flying below the F2 region peak height to encounter low-density region. Furthermore, Figure 9 shows an equatorial ionosonde measurement of Ne profile and F2-layer peak height (hmF2) at GUAM between January 13–16, 2022. As can be seen, GUAM hmF2 exhibited a strong postsunset rise (PSSR) to 440 km at ~09 UT on January 15 around the anticipated arrival time of volcano-induced atmospheric Lamb waves as marked by a white arrow. This postsunset rise of F-layer was 60–80 km considerably larger than that of other reference days. The IMF Bz/By and IEF had merely limited variations around this time, indicating a weak PEF effect. Such a large enhancement of PRE magnitude and postsunset rise of equatorial ionospheric F-layer led to increased R-T instability growth rate and thus contributed to vigorous EPBs that were shown in ICON-IVM and Swarm in situ measurements. Moreover, Figure 8f displays the time-distance variation of ROTI values with the equatorial sunset terminator and Lamb wave propagation trend being marked. As can be seen, the equatorial dusk terminator and Lamb wave swept over the wide Asia-Oceania area almost simultaneously or consecutively since ~06:30 UT, which provides a favorable background condition with increased PRE and Rayleigh-Taylor instability growth rate under the right timing of direct AGWs seeding induced by the volcanic eruption. The longitudinal extension of these strong EPBs was over 140°, which is

slightly smaller but comparable to the longitudinal extension of volcano-induced TIDs (Zhang et al., 2022). This provides further evidence to support the connection between these strong EPBs and volcano-induced AGWs.

In aggregate, these volcano-related factors could work together to catalyze and amplify initial plasma density perturbations as well as to contribute to increased PRE/PSSR and Rayleigh-Taylor instability growth rate, which effectively facilitated the development of pronounced and extensive EPBs over wide Asia-Oceania longitudes following the consecutive passage of sunset terminator and atmospheric Lamb waves. The storm-modified electric field might provide a partial contribution. Future simulation work is needed to investigate further this significant EPB event with surface-to-ionosphere connections, which is beyond the scope of the current observation study.

5. Conclusions

Local and global ionospheric disturbances associated with the 2022 Tonga volcano eruption were studied using both ground-based and space-borne observations, including Beidou GEO TEC from fixed IPPs, multi-GNSS ROTI data, Swarm and ICON in situ measurements, as well as ionosonde measurements. The main results and findings are as follows:

1. The volcano eruption resulted in a significant local ionospheric hole of more than 10 TECU near the epicenter that consisted of cascading TEC decreases and oscillations. The horizontal radius of this plasma hole was estimated to be around 10–15°. This could be explained by strong thermosphere expansion and large ionosphere outward flow driven by consecutive intense co-volcanic shock-acoustic wave impulses. This plasma hole signature persisted for more than 10 hr in ICON-IVM plasma density profiles until local sunrise, likely due to a shortage of nighttime photo-ionization sources with low background density levels.
2. We observed both local and distant ionospheric large-amplitude disturbances due to various volcano-induced AGW modes with different phase velocities, including fast acoustic modes of ∼1050 m/s and ∼760 m/s, infrasonic mode of ∼460 m/s, atmospheric Lamb waves mode of ∼315 m/s, and tsunami-gravity modes of ∼180–250 m/s. The atmospheric Lamb waves mode exhibited the most distinct long-distance traveling feature reaching at least 16,000 km away from the epicenter, causing significant global-scale ionospheric disturbances via acoustic-gravity resonance and wave coupling.
3. For the first time, we observed pronounced equatorial plasma trough and prolonged post-volcanic evening plasma bubbles over the Asia-Oceania area, following the volcano-eruption that was associated with enhanced dusktime upward plasma drifts of 60–120 m/s. The observed plasma bubbles continuously developed across a wide longitudinal area at an approximate Lamb wave velocity over 140° and lasted around 12 hr, with plasma density decreased by 2–3 orders of magnitude at Swarm/ICON altitude between 450 and 575 km. Given that the dusk terminator and westbound propagating Lamb waves swept over the Asia-Oceania area consecutively, significant plasma bubbles were likely seeded by gravity resonance and coupling with less-damped Lamb waves, under the right timing with favorable background conditions of largely increased PRE and postsunset rise of equatorial F-layer to effectively amplify the Rayleigh-Taylor instability growth rate via volcano-induced AGWs. The storm-modified electric field could also play a secondary role though its specific contribution needs future investigation.

Data Availability Statement

Global Navigation Satellite System TEC data products are provided through the Madrigal distributed data system at (http://cedar.openmadrigal.org/) by MIT. Swarm data are provided by European Space Agency (https://swarm-diss.eo.esa.int/). The ICON data can be accessed at (https://icon.ssl.berkeley.edu/Data). The cloud brightness temperature data are provided by NASA Goddard Earth Sciences Data and Information Services Central (https://disc.gsfc.nasa.gov/datasets/GPM_MERGIR_1/summary). The solar wind and geophysical parameters data is acquired from NASA/GSFC's Space Physics Data Facility's OMNIWeb service (https://cdaweb.gsfc.nasa.gov/) and Kyoto world data center for Geomagnetism (http://wdc.kugi.kyoto-u.ac.jp/).

Acknowledgments
Global Navigation Satellite System TEC data are part of the U.S. NSF's Millstone Hill Geospace Facility program under AGS-1952737 with MIT. We acknowledge NSF awards AGS-2033787 and PHY-2028125, NASA support 80NSSC22K0171, 80NSSC21K1310, 80NSSC21K1775, and 80NSSC19K0834, AFOSR MURI Project FA9559-16-1-0364, and ONR Grant N00014-17-1-2186. Data for TEC processing is provided from the following organizations: UNAVCO, SOPAC, IGN (France), IGS, CDDIS, NGS, IBGE (Brazil), RAMSAC (Argentina), CORS (Panama), Arecibo Observatory, LISN, Topcon, CHAIN (Canada), CRS (Italy), SONEL, RENAG (New Zealand), GNSS Reference Networks, Finnish Meteorological Institute, and SWEPOS.

References

Aa, E., Zhang, S.-R., Wang, W., Erickson, P. J., Qian, L., Eastes, R., et al. (2022). Pronounced Suppression and X-Pattern Merging of Equatorial Ionization Anomalies After the 2022 Tonga Volcano Eruption. *Journal of Geophysical Research: Space Physics*, *127*(6), e2022JA030527. https://doi.org/10.1029/2022JA030527

Aa, E., Zou, S., Eastes, R., Karan, D. K., Zhang, S.-R., Erickson, P. J., & Coster, A. J. (2020). Coordinated ground-based and space-based observations of equatorial plasma bubbles. *Journal of Geophysical Research: Space Physics*, *125*(1), e27569. https://doi.org/10.1029/2019JA027569

Aa, E., Zou, S., & Liu, S. (2020). Statistical analysis of equatorial plasma irregularities retrieved from Swarm 2013–2019 observations. *Journal of Geophysical Research: Space Physics*, *125*(4), e27022. https://doi.org/10.1029/2019JA027022

Aa, E., Zou, S., Ridley, A., Zhang, S., Coster, A. J., Erickson, P. J., et al. (2019). Merging of storm time midlatitude traveling ionospheric disturbances and equatorial plasma bubbles. *Space Weather*, *17*(2), 285–298. https://doi.org/10.1029/2018SW002101

Abdu, M. A. (2005). Equatorial ionosphere thermosphere system: Electrodynamics and irregularities. *Advances in Space Research*, *35*(5), 771–787. https://doi.org/10.1016/j.asr.2005.03.150

Abdu, M. A., Alam Kherani, E., Batista, I. S., de Paula, E. R., Fritts, D. C., & Sobral, J. H. A. (2009). Gravity wave initiation of equatorial spread F/plasma bubble irregularities based on observational data from the SpreadFEx campaign. *Annales Geophysicae*, *27*(7), 2607–2622. https://doi.org/10.5194/angeo-27-2607-2009

Afraimovich, E. L., Feng, D., Kiryushkin, V. V., & Astafyeva, E. I. (2010). Near-field TEC response to the main shock of the 2008 Wenchuan earthquake. *Earth Planets and Space*, *62*(11), 899–904. https://doi.org/10.5047/eps.2009.07.002

Artru, J., Ducic, V., Kanamori, H., Lognonné, P., & Murakami, M. (2005). Ionospheric detection of gravity waves induced by tsunamis. *Geophysical Journal International*, *160*(3), 840–848. https://doi.org/10.1111/j.1365-246X.2005.02552.x

Artru, J., Farges, T., & Lognonné, P. (2004). Acoustic waves generated from seismic surface waves: Propagation properties determined from Doppler sounding observations and normal-mode modelling. *Geophysical Journal International*, *158*(3), 1067–1077. https://doi.org/10.1111/j.1365-246X.2004.02377.x

Astafyeva, E. (2019). Ionospheric detection of natural hazards. *Reviews of Geophysics*, *57*(4), 1265–1288. https://doi.org/10.1029/2019RG000668

Astafyeva, E., Maletckii, B., Mikesell, T. D., Munaibari, E., Ravenelli, M., Coisson, P., et al. (2022). The 15 January 2022 Hunga Tonga eruption history as inferred from ionospheric observations. *Earth and Space Science Open Archive*. https://doi.org/10.1002/essoar.10511226.1

Astafyeva, E., Shalimov, S., Olshanskaya, E., & Lognonné, P. (2013). Ionospheric response to earthquakes of different magnitudes: Larger quakes perturb the ionosphere stronger and longer. *Geophysical Research Letters*, *40*(9), 1675–1681. https://doi.org/10.1002/grl.50398

Azeem, I., Vadas, S. L., Crowley, G., & Makela, J. J. (2017). Traveling ionospheric disturbances over the United States induced by gravity waves from the 2011 Tohoku tsunami and comparison with gravity wave dissipative theory. *Journal of Geophysical Research: Space Physics*, *122*(3), 3430–3447. https://doi.org/10.1002/2016JA023659

Blanc, E. (1985). Observations in the upper atmosphere of infrasonic waves from natural or artificial sources—A summary. *Annales Geophysicae*, *3*, 673–687.

Blanc, M., & Richmond, A. D. (1980). The ionospheric disturbance dynamo. *Journal of Geophysical Research*, *85*(A4), 1669–1686. https://doi.org/10.1029/JA085iA04p01669

Bretherton, F. P. (1969). Lamb waves in a nearly isothermal atmosphere. *Quarterly Journal of the Royal Meteorological Society*, *95*(406), 754–757. https://doi.org/10.1002/qj.49709540608

Burke, W. J., Gentile, L. C., Huang, C. Y., Valladares, C. E., & Su, S. Y. (2004). Longitudinal variability of equatorial plasma bubbles observed by DMSP and ROCSAT-1. *Journal of Geophysical Research*, *109*(A12), A12301. https://doi.org/10.1029/2004JA010583

Cahyadi, M. N., & Heki, K. (2013). Ionospheric disturbances of the 2007 Bengkulu and the 2005 Nias earthquakes, Sumatra, observed with a regional GPS network. *Journal of Geophysical Research: Space Physics*, *118*(4), 1777–1787. https://doi.org/10.1002/jgra.50208

Calais, E., Bernard Minster, J., Hofton, M., & Hedlin, M. (1998). Ionospheric signature of surface mine blasts from Global Positioning System measurements. *Geophysical Journal International*, *132*(1), 191–202. https://doi.org/10.1046/j.1365-246X.1998.00438.x

Carter, B. A., Yizengaw, E., Pradipta, R., Retterer, J. M., Groves, K., Valladares, C., et al. (2016). Global equatorial plasma bubble occurrence during the 2015 St. Patrick's Day storm. *Journal of Geophysical Research: Space Physics*, *121*(1), 894–905. https://doi.org/10.1002/2015JA022194

Chen, C. H., Saito, A., Lin, C. H., Liu, J. Y., Tsai, H. F., Tsugawa, T., et al. (2011). Long-distance propagation of ionospheric disturbance generated by the 2011 off the Pacific coast of Tohoku Earthquake. *Earth Planets and Space*, *63*(7), 881–884. https://doi.org/10.5047/eps.2011.06.026

Cherniak, I., Krankowski, A., & Zakharenkova, I. (2014). Observation of the ionospheric irregularities over the northern hemisphere: Methodology and service. *Radio Science*, *49*(8), 653–662. https://doi.org/10.1002/2014RS005433

Cherniak, I., & Zakharenkova, I. (2016). First observations of super plasma bubbles in Europe. *Geophysical Research Letters*, *43*(21), 11137–11145. https://doi.org/10.1002/2016GL071421

Chou, M.-Y., Cherniak, I., Lin, C. C. H., & Pedatella, N. M. (2020). The persistent ionospheric responses over Japan after the impact of the 2011 Tohoku earthquake. *Space Weather*, *18*(4), e02302. https://doi.org/10.1029/2019SW002302

Das, S. K., Patra, A. K., Kherani, E. A., Chaitanya, P. P., & Niranjan, K. (2020). Relationship between presunset wave structures and interbubble spacing: The seeding perspective of equatorial plasma bubble. *Journal of Geophysical Research: Space Physics*, *125*(8), e28122. https://doi.org/10.1029/2020JA028122

Dautermann, T., Calais, E., Lognonné, P., & Mattioli, G. S. (2009). Lithosphere-atmosphere-ionosphere coupling after the 2003 explosive eruption of the Soufriere hills volcano, Montserrat. *Geophysical Journal International*, *179*(3), 1537–1546. https://doi.org/10.1111/j.1365-246X.2009.04390.x

Dautermann, T., Calais, E., & Mattioli, G. S. (2009). Global Positioning System detection and energy estimation of the ionospheric wave caused by the 13 July 2003 explosion of the Soufrière Hills Volcano, Montserrat. *Journal of Geophysical Research*, *114*(B2), B02202. https://doi.org/10.1029/2008JB005722

Duncombe, J. (2022). The surprising reach of Tonga's giant atmospheric waves. *Eos: AGU Science News*, *103*. https://doi.org/10.1029/2022EO220050

Eccles, J. V., St. Maurice, J. P., & Schunk, R. W. (2015). Mechanisms underlying the prereversal enhancement of the vertical plasma drift in the low-latitude ionosphere. *Journal of Geophysical Research: Space Physics*, *120*(6), 4950–4970. https://doi.org/10.1002/2014JA020664

Foster, J. C., & Rich, F. J. (1998). Prompt midlatitude electric field effects during severe geomagnetic storms. *Journal of Geophysical Research*, *103*(A11), 26367–26372. https://doi.org/10.1029/97JA03057

Friis-Christensen, E., Lühr, H., Knudsen, D., & Haagmans, R. (2008). Swarm-an Earth observation mission investigating Geospace. *Advances in Space Research*, *41*(1), 210–216. https://doi.org/10.1016/j.asr.2006.10.008

Fritts, D. C., Vadas, S. L., Riggin, D. M., Abdu, M. A., Batista, I. S., Takahashi, H., et al. (2008). Gravity wave and tidal influences on equatorial spread F based on observations during the Spread F Experiment (SpreadFEx). *Annales Geophysicae*, *26*(11), 3235–3252. https://doi.org/10.5194/angeo-26-3235-2008

Hao, Y.-Q., Xiao, Z., & Zhang, D.-H. (2006). Responses of the ionosphere to the great Sumatra earthquake and volcanic eruption of Pinatubo. *Chinese Physics Letters*, *23*(7), 1955–1957. https://doi.org/10.1088/0256-307X/23/7/082

Harding, B. J., Wu, Y.-J. J., Alken, P., Yamazaki, Y., Triplett, C. C., Immel, T. J., et al. (2022). Impacts of the January 2022 Tonga volcanic eruption on the ionospheric dynamo: ICON-MIGHTI and Swarm observations of extreme neutral winds and currents. *Geophysical Research Letters*, *49*(9), e2022GL098577. https://doi.org/10.1029/2022GL098577

Heelis, R. A., Stoneback, R. A., Perdue, M. D., Depew, M. D., Morgan, W. A., Mankey, M. W., et al. (2017). Ion velocity measurements for the ionospheric connections explorer. *Space Science Reviews*, *212*(1–2), 615–629. https://doi.org/10.1007/s11214-017-0383-3

Heki, K. (2006). Explosion energy of the 2004 eruption of the Asama Volcano, central Japan, inferred from ionospheric disturbances. *Geophysical Research Letters*, *33*(14), L14303. https://doi.org/10.1029/2006GL026249

Heki, K., & Ping, J. (2005). Directivity and apparent velocity of the coseismic ionospheric disturbances observed with a dense GPS array. *Earth and Planetary Science Letters*, *236*(3–4), 845–855. https://doi.org/10.1016/j.epsl.2005.06.010

Hines, C. O. (1960). Internal atmospheric gravity waves at ionospheric heights. *Canadian Journal of Physics*, *38*(11), 1441–1481. https://doi.org/10.1139/p60-150

Huang, C.-S., & Kelley, M. C. (1996). Nonlinear evolution of equatorial spread F. 1. On the role of plasma instabilities and spatial resonance associated with gravity wave seeding. *Journal of Geophysical Research*, *101*(A1), 283–292. https://doi.org/10.1029/95JA02211

Huang, C. Y., Helmboldt, J. F., Park, J., Pedersen, T. R., & Willemann, R. (2019). Ionospheric detection of explosive events. *Reviews of Geophysics*, *57*(1), 78–105. https://doi.org/10.1029/2017RG000594

Huba, J. D., Drob, D. P., Wu, T. W., & Makela, J. J. (2015). Modeling the ionospheric impact of tsunami-driven gravity waves with SAMI3: Conjugate effects. *Geophysical Research Letters*, *42*(14), 5719–5726. https://doi.org/10.1002/2015GL064871

Huba, J. D., & Liu, H. L. (2020). Global modeling of equatorial spread F with SAMI3/WACCM-X. *Geophysical Research Letters*, *47*(14), e88258. https://doi.org/10.1029/2020GL088258

Hysell, D. L., Kelley, M. C., Swartz, W. E., & Woodman, R. F. (1990). Seeding and layering of equatorial spread F by gravity waves. *Journal of Geophysical Research*, *95*(A10), 17253–17260. https://doi.org/10.1029/JA095iA10p17253

Immel, T. J., England, S. L., Mende, S. B., Heelis, R. A., Englert, C. R., Edelstein, J., et al. (2018). The ionospheric connection explorer mission: Mission goals and design. *Space Science Reviews*, *214*(1), 13. https://doi.org/10.1007/s11214-017-0449-2

Inchin, P. Â. A., Snively, J. Â. B., Zettergren, M. Â. D., Komjathy, A., Verkhoglyadova, O. Â. P., & Tulasi Ram, S. (2020). Modeling of ionospheric responses to atmospheric acoustic and gravity waves driven by the 2015 Nepal Mw7.8 gorkha earthquake. *Journal of Geophysical Research: Space Physics*, *125*(4), e27200. https://doi.org/10.1029/2019JA027200

Janowiak, J., Joyce, B., & Xie, P. (2017). *Ncep/cpc l3 half hourly 4km global (60s—60n) merged ir v1*. NASA Goddard Earth Sciences Data and Information Services Center. https://doi.org/10.5067/P4HZB9N27EKU

Jin, H., Zou, S., Chen, G., Yan, C., Zhang, S., & Yang, G. (2018). formation and evolution of low-latitude F region field-aligned irregularities during the 7–8 September 2017 storm: Hainan coherent scatter phased array radar and digisonde observations. *Space Weather*, *16*(6), 648–659. https://doi.org/10.1029/2018SW001865

Kakinami, Y., Kamogawa, M., Tanioka, Y., Watanabe, S., Riadi Gusman, A., Liu, J.-Y., & Mogi, T. (2012). Tsunamigenic ionospheric hole. *Geophysical Research Letters*, *39*(13), L00G27. https://doi.org/10.1029/2011GL050159

Kamogawa, M., Kanaya, T., Orihara, Y., Toyoda, A., Suzuki, Y., Togo, S., & Liu, J.-Y. (2015). Does an ionospheric hole appear after an inland earthquake? *Journal of Geophysical Research: Space Physics*, *120*(11), 9998–10. https://doi.org/10.1002/2015JA021476

Karan, D. K., Daniell, R. E., England, S. L., Martinis, C. R., Eastes, R. W., Burns, A. G., & McClintock, W. E. (2020). First zonal drift velocity measurement of equatorial plasma bubbles (EPBs) from a geostationary orbit using GOLD data. *Journal of Geophysical Research: Space Physics*, *125*(9), e28173. https://doi.org/10.1029/2020JA028173

Katamzi-Joseph, Z. T., Habarulema, J. B., & Hernández-Pajares, M. (2017). Midlatitude postsunset plasma bubbles observed over Europe during intense storms in April 2000 and 2001. *Space Weather*, *15*(9), 1177–1190. https://doi.org/10.1002/2017SW001674

Kelley, M. C., Haerendel, G., Kappler, H., Valenzuela, A., Balsley, B. B., Carter, D. A., et al. (1976). Evidence for a Rayleigh-Taylor type instability and upwelling of depleted density regions during equatorial spread F. *Geophysical Research Letters*, *3*(8), 448–450. https://doi.org/10.1029/GL003i008p00448

Kil, H., & Lee, W. K. (2013). Are plasma bubbles a prerequisite for the formation of broad plasma depletions in the equatorial F region? *Geophysical Research Letters*, *40*(14), 3491–3495. https://doi.org/10.1002/grl.50693

Kil, H., Paxton, L. J., & Oh, S.-J. (2009). Global bubble distribution seen from ROCSAT-1 and its association with the evening prereversal enhancement. *Journal of Geophysical Research*, *114*(A6), A06307. https://doi.org/10.1029/2008JA013672

Knudsen, D. J., Burchill, J. K., Buchert, S. C., Eriksson, A. I., Gill, R., Wahlund, J. E., et al. (2017). Thermal ion imagers and Langmuir probes in the Swarm electric field instruments. *Journal of Geophysical Research: Space Physics*, *122*(2), 2655–2673. https://doi.org/10.1002/2016JA022571

Komjathy, A., Galvan, D. A., Stephens, P., Butala, M. D., Akopian, V., Wilson, B., et al. (2012). Detecting ionospheric TEC perturbations caused by natural hazards using a global network of GPS receivers: The Tohoku case study. *Earth Planets and Space*, *64*(12), 1287–1294. https://doi.org/10.5047/eps.2012.08.003

Komjathy, A., Yang, Y.-M., Meng, X., Verkhoglyadova, O., Mannucci, A. J., & Langley, R. B. (2016). Review and perspectives: Understanding natural-hazards-generated ionospheric perturbations using gps measurements and coupled modeling. *Radio Science*, *51*(7), 951–961. https://doi.org/10.1002/2015RS005910

Krall, J., Huba, J. D., & Fritts, D. C. (2013). On the seeding of equatorial spread F by gravity waves. *Geophysical Research Letters*, *40*(4), 661–664. https://doi.org/10.1002/grl.50144

Kudeki, E., Akgiray, A., Milla, M., Chau, J. L., & Hysell, D. L. (2007). Equatorial spread-F initiation: Post-sunset vortex, thermospheric winds, gravity waves. *Journal of Atmospheric and Solar-Terrestrial Physics*, *69*(17–18), 2416–2427. https://doi.org/10.1016/j.jastp.2007.04.012

Le, G., Liu, G., Yizengaw, E., & Englert, C. (2022). Intense equatorial electrojet and counter electrojet caused by the 15 January 2022 Tonga volcanic eruption: Space and ground-based observations. *Earth and Space Science Open Archive*. https://doi.org/10.1002/essoar.10511040.2

Lee, W. K., Kil, H., Kwak, Y.-S., Paxton, L. J., Zhang, Y., Galkin, I., & Batista, I. S. (2014). Equatorial broad plasma depletions associated with the enhanced fountain effect. *Journal of Geophysical Research: Space Physics*, *119*(1), 402–410. https://doi.org/10.1002/2013JA019137

Li, G., Ning, B., Liu, L., Wan, W., & Liu, J. Y. (2009). Effect of magnetic activity on plasma bubbles over equatorial and low-latitude regions in East Asia. *Annales Geophysicae*, *27*(1), 303–312. https://doi.org/10.5194/angeo-27-303-2009

Lin, J.-T., Rajesh, P. K., Lin, C. C. H., Chou, M.-Y., Liu, J.-Y., Yue, J., et al. (2022). Rapid conjugate appearance of the giant ionospheric lamb wave in the northern hemisphere after Hunga-Tonga volcano eruptions. *Earth and Space Science Open Archive*, *18*. https://doi.org/10.1002/essoar.10510440.2

Lindzen, R. S., & Blake, D. (1972). Lamb waves in the presence of realistic distributions of temperature and dissipation. *Journal of Geophysical Research*, *77*(12), 2166–2176. https://doi.org/10.1029/JC077i012p02166

Liu, C. H., Klostermeyer, J., Yeh, K. C., Jones, T. B., Robinson, T., Holt, O., et al. (1982). Global dynamic responses of the atmosphere to the eruption of Mount St. Helens on May 18, 1980. *Journal of Geophysical Research*, *87*(A8), 6281–6290. https://doi.org/10.1029/JA087iA08p06281

Liu, J. Y., Tsai, Y. B., Chen, S. W., Lee, C. P., Chen, Y. C., Yen, H. Y., et al. (2006). Giant ionospheric disturbances excited by the M9.3 Sumatra earthquake of 26 December 2004. *Geophysical Research Letters*, *33*(2), L02103. https://doi.org/10.1029/2005GL023963

Ma, G., & Maruyama, T. (2006). A super bubble detected by dense GPS network at East Asian longitudes. *Geophysical Research Letters*, *33*(21), L21103. https://doi.org/10.1029/2006GL027512

Makela, J. J., Vadas, S. L., Muryanto, R., Duly, T., & Crowley, G. (2010). Periodic spacing between consecutive equatorial plasma bubbles. *Geophysical Research Letters*, *37*(14), L14103. https://doi.org/10.1029/2010GL043968

Meng, X., Verkhoglyadova, O. P., Komjathy, A., Savastano, G., & Mannucci, A. J. (2018). Physics-based modeling of earthquake-induced ionospheric disturbances. *Journal of Geophysical Research: Space Physics*, *123*(9), 8021–8038. https://doi.org/10.1029/2018JA025253

Nakashima, Y., Heki, K., Takeo, A., Cahyadi, M. N., Aditiya, A., & Yoshizawa, K. (2016). Atmospheric resonant oscillations by the 2014 eruption of the Kelud volcano, Indonesia, observed with the ionospheric total electron contents and seismic signals. *Earth and Planetary Science Letters*, *434*, 112–116. https://doi.org/10.1016/j.epsl.2015.11.029

Nishida, K., Kobayashi, N., & Fukao, Y. (2014). Background Lamb waves in the Earth's atmosphere. *Geophysical Journal International*, *196*(1), 312–316. https://doi.org/10.1093/gji/ggt413

Nishioka, M., Tsugawa, T., Kubota, M., & Ishii, M. (2013). Concentric waves and short-period oscillations observed in the ionosphere after the 2013 Moore EF5 Tornado. *Geophysical Research Letters*, *40*(21), 5581–5586. https://doi.org/10.1002/2013GL057963

Otsuka, Y., Kotake, N., Tsugawa, T., Shiokawa, K., Ogawa, T., Effendy, et al. (2006). GPS detection of total electron content variations over Indonesia and Thailand following the 26 December 2004 earthquake. *Earth Planets and Space*, *58*(2), 159–165. https://doi.org/10.1186/BF03353373

Pi, X., Mannucci, A. J., Lindqwister, U. J., & Ho, C. M. (1997). Monitoring of global ionospheric irregularities using the Worldwide GPS Network. *Geophysical Research Letters*, *24*(18), 2283–2286. https://doi.org/10.1029/97GL02273

Retterer, J. M., & Roddy, P. (2014). Faith in a seed: On the origins of equatorial plasma bubbles. *Annales Geophysicae*, *32*(5), 485–498. https://doi.org/10.5194/angeo-32-485-2014

Rideout, W., & Coster, A. (2006). Automated GPS processing for global total electron content data. *GPS Solutions*, *10*(3), 219–228. https://doi.org/10.1007/s10291-006-0029-5

Rishbeth, H. (1971). The F-layer dynamo. *Planetary and Space Science*, *19*(2), 263–267. https://doi.org/10.1016/0032-0633(71)90205-4

Roberts, D. H., Klobuchar, J. A., Fougere, P. F., & Hendrickson, D. H. (1982). A large-amplitude traveling ionospheric disturbance produced by the May 18, 1980, explosion of Mount St. Helens. *Journal of Geophysical Research*, *87*(A8), 6291–6301. https://doi.org/10.1029/JA087iA08p06291

Rolland, L. M., Lognonné, P., Astafyeva, E., Kherani, E. A., Kobayashi, N., Mann, M., & Munekane, H. (2011). The resonant response of the ionosphere imaged after the 2011 off the Pacific coast of Tohoku Earthquake. *Earth Planets and Space*, *63*(7), 853–857. https://doi.org/10.5047/eps.2011.06.020

Rottger, J. (1981). Equatorial spread-F by electric fields and atmospheric gravity waves generated by thunderstorms. *Journal of Atmospheric and Terrestrial Physics*, *43*(5–6), 453–462. https://doi.org/10.1016/0021-9169(81)90108-2

Saito, A., Tsugawa, T., Otsuka, Y., Nishioka, M., Iyemori, T., Matsumura, M., et al. (2011). Acoustic resonance and plasma depletion detected by GPS total electron content observation after the 2011 off the Pacific coast of Tohoku Earthquake. *Earth Planets and Space*, *63*(7), 863–867. https://doi.org/10.5047/eps.2011.06.034

Savastano, G., Komjathy, A., Verkhoglyadova, O., Mazzoni, A., Crespi, M., Wei, Y., & Mannucci, A. J. (2017). Real-time detection of tsunami ionospheric disturbances with a stand-alone GNSS receiver: A preliminary feasibility demonstration. *Scientific Reports*, *7*(1), 46607. https://doi.org/10.1038/srep46607

Savitzky, A., & Golay, M. J. E. (1964). Smoothing and differentiation of data by simplified least squares procedures. *Analytical Chemistry*, *36*(8), 1627–1639. https://doi.org/10.1021/ac60214a047

Shinagawa, H., Tsugawa, T., Matsumura, M., Iyemori, T., Saito, A., Maruyama, T., et al. (2013). Two-dimensional simulation of ionospheric variations in the vicinity of the epicenter of the Tohoku-Oki earthquake on 11 March 2011. *Geophysical Research Letters*, *40*(19), 5009–5013. https://doi.org/10.1002/2013GL057627

Shiokawa, K., Otsuka, Y., Ogawa, T., & Wilkinson, P. (2004). Time evolution of high-altitude plasma bubbles imaged at geomagnetic conjugate points. *Annales Geophysicae*, *22*(9), 3137–3143. https://doi.org/10.5194/angeo-22-3137-2004

Shults, K., Astafyeva, E., & Adourian, S. (2016). Ionospheric detection and localization of volcano eruptions on the example of the April 2015 Calbuco events. *Journal of Geophysical Research: Space Physics*, *121*(10), 10303–10315. https://doi.org/10.1002/2016JA023382

Singh, S., Johnson, F. S., & Power, R. A. (1997). Gravity wave seeding of equatorial plasma bubbles. *Journal of Geophysical Research*, *102*(A4), 7399–7410. https://doi.org/10.1029/96JA03998

Spicher, A., Cameron, T., Grono, E. M., Yakymenko, K. N., Buchert, S. C., Clausen, L. B. N., et al. (2015). Observation of polar cap patches and calculation of gradient drift instability growth times: A Swarm case study. *Geophysical Research Letters*, *42*(2), 201–206. https://doi.org/10.1002/2014GL062590

Sultan, P. J. (1996). Linear theory and modeling of the Rayleigh-Taylor instability leading to the occurrence of equatorial spread F. *Journal of Geophysical Research*, *101*(A12), 26875–26892. https://doi.org/10.1029/96JA00682

Takahashi, H., Taylor, M. J., Pautet, P. D., Medeiros, A. F., Gobbi, D., Wrasse, C. M., et al. (2009). Simultaneous observation of ionospheric plasma bubbles and mesospheric gravity waves during the SpreadFEx Campaign. *Annales Geophysicae*, *27*(4), 1477–1487. https://doi.org/10.5194/angeo-27-1477-2009

Takahashi, H., Wrasse, C. M., Otsuka, Y., Ivo, A., Gomes, V., Paulino, I., et al. (2015). Plasma bubble monitoring by TEC map and 630 nm airglow image. *Journal of Atmospheric and Solar-Terrestrial Physics*, *130*, 151–158. https://doi.org/10.1016/j.jastp.2015.06.003

Themens, D. R., Watson, C., Žagar, N., Vasylkevych, S., Elvidge, S., McCaffrey, A., et al. (2022). Global propagation of ionospheric disturbances associated with the 2022 Tonga volcanic eruption. *Geophysical Research Letters*, *49*(7), e2022GL098158. https://doi.org/10.1029/2022GL098158

Tsugawa, T., Saito, A., Otsuka, Y., Nishioka, M., Maruyama, T., Kato, H., et al. (2011). Ionospheric disturbances detected by GPS total electron content observation after the 2011 off the Pacific coast of Tohoku Earthquake. *Earth Planets and Space*, *63*(7), 875–879. https://doi.org/10.5047/eps.2011.06.035

Tsunoda, R. T. (2010). On seeding equatorial spread F: Circular gravity waves. *Geophysical Research Letters*, *37*(10), L10104. https://doi.org/10.1029/2010GL043422

Tsunoda, R. T., Yamamoto, M., Tsugawa, T., Hoang, T. L., Tulasi Ram, S., Thampi, S. V., et al. (2011). On seeding, large-scale wave structure, equatorial spread F, and scintillations over Vietnam. *Geophysical Research Letters*, *38*(20), L20102. https://doi.org/10.1029/2011GL049173

Tulasi Ram, S., Rama Rao, P. V. S., Prasad, D. S. V. V. D., Niranjan, K., Gopi Krishna, S., Sridharan, R., & Ravindran, S. (2008). Local time dependent response of postsunset ESF during geomagnetic storms. *Journal of Geophysical Research*, *113*(A7), A07310. https://doi.org/10.1029/2007JA012922

Vierinen, J., Coster, A. J., Rideout, W. C., Erickson, P. J., & Norberg, J. (2016). Statistical framework for estimating GNSS bias. *Atmospheric Measurement Techniques*, *9*(3), 1303–1312. https://doi.org/10.5194/amt-9-1303-2016

Yeh, K. C., & Liu, C. H. (1974). Acoustic-gravity waves in the upper atmosphere. *Reviews of Geophysics and Space Physics*, *12*(2), 193. https://doi.org/10.1029/RG012i002p00193

Zakharenkova, I., Cherniak, I., & Krankowski, A. (2019). Features of storm-induced ionospheric irregularities from ground-based and spaceborne GPS observations during the 2015 St. Patrick's day storm. *Journal of Geophysical Research: Space Physics*, *124*(12), 10728–10748. https://doi.org/10.1029/2019JA026782

Zettergren, M. D., Snively, J. B., Komjathy, A., & Verkhoglyadova, O. P. (2017). Nonlinear ionospheric responses to large-amplitude infrasonic-acoustic waves generated by undersea earthquakes. *Journal of Geophysical Research: Space Physics*, *122*(2), 2272–2291. https://doi.org/10.1002/2016JA023159

Zhang, S.-R., Erickson, P. J., Coster, A. J., Rideout, W., Vierinen, J., Jonah, O., & Goncharenko, L. P. (2019). Subauroral and polar traveling ionospheric disturbances during the 7–9 September 2017 storms. *Space Weather*, *17*(12), 1748–1764. https://doi.org/10.1029/2019SW002325

Zhang, S.-R., Erickson, P. J., Goncharenko, L. P., Coster, A. J., Rideout, W., & Vierinen, J. (2017). Ionospheric bow waves and perturbations induced by the 21 August 2017 solar eclipse. *Geophysical Research Letters*, *44*(24), 12067–12073. https://doi.org/10.1002/2017GL076054

Zhang, S.-R., Vierinen, J., Aa, E., Goncharenko, L. P., Erickson, P. J., Rideout, W., et al. (2022). 2022 Tonga volcanic eruption induced global propagation of ionospheric disturbances via Lamb waves. *Frontiers in Astronomy and Space Sciences*, *15*. https://doi.org/10.3389/fspas.2022.871275